Multiple Moving Target Detection and Trajectory Estimation Using a Single SAR Sensor

José M. B. Dias and Paulo A. C. Marques

Abstract— **The paper presents a novel methodology for determining the velocity and location of multiple moving targets using a single stripmap synthetic aperture radar (SAR) sensor. The so-called *azimuth position uncertainty problem* is therefore solved. The method exploits the structure of the amplitude and phase modulations of the returned echo from a moving target in the Fourier domain. A crucial step in the whole processing scheme is a matched filtering, depending on the moving target parameters, that simultaneously accounts for range migration and compresses two-dimensional signatures into one-dimensional ones without loosing moving target information. A generalized likelihood ratio test approach is adopted to detect moving targets and derive their trajectory parameters. The effectiveness of the method is illustrated with synthetic and real data covering a wide range of targets velocities and signal to clutter ratios (SCRs). Even in the case of parallel to platform moving target motion, the most unfavorable scenario, the proposed method yields good results for, roughly, SCR> 10 dB.**

Keywords—**Synthetic aperture radar, azimuth position uncertainty problem, multiple moving targets, trajectory parameter estimation, range migration, generalized likelihood ratio test.**

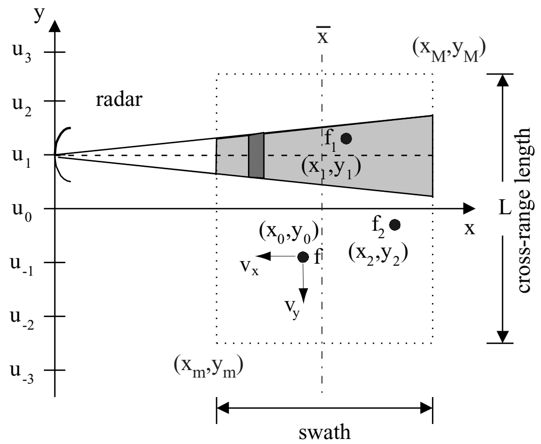

Fig. 1. Typical stripmap SAR scenario.

I. Introduction

FIGURE 1 shows the slant-plane of a typical stripmap synthetic aperture radar (SAR) scenario (coordinate x denotes slant-range, i.e., broadside distance measured from the radar). A radar travelling at constant altitude and constant velocity along the flight path (cross-range direction) transmits microwave pulses at regular intervals and records the backscattered echoes. The illuminated scene might contain static and moving targets. High resolution in the slant-range direction is achieved by pulse compression techniques, whereas high resolution in the cross-range direction is achieved by synthesizing a large aperture, exploiting the relative motion between the platform and the illuminated scene [1].

The need for detecting moving targets and estimating their trajectories appears in many SAR applications [2], [3], [4], [5], [6], [7]. For example, properly moving target focusing and locating requires the knowledge of the respective velocity vector (i.e., cross-range and slant-range velocity components) [7, ch. 6.7]. If the moving target returns are processed in the same way as the static returns, the resulting SAR image shows the former defocused and/or at wrong positions, depending on the motion direction [2], [8]. Roughly, a moving target in the cross-range direction appears blurred, whereas a moving target in the slant-range direction appears misplaced.

Several methods have been proposed to detect and focus moving targets using a single antenna. Most of them are based on the cross-range phase history originated by moving targets (e.g., [3], [4], [5], [9], [10, ch. 5], [11], [12]). However, the cross-range phase history originated by a point moving target with constant velocity is characterized only by two parameters [2]: the Doppler shift and the Doppler rate. The latter gives the velocity magnitude and is required for correct focusing, whereas the former depends on the projection of the relative velocity along the radar-target line of sight [4], [10, ch. 4]. Therefore, from the cross-range phase history of a moving target it is not possible to infer the exact direction of its velocity vector, making it impossible to correctly locate the moving target image. This limitation is termed *azimuth position uncertainty* [4] or *blind angle ambiguity* [5], [7]. Both, Soumekh in [10, ch. 5] and Barbarossa in [4] state that unless stereo measures are available, it is not possible to determine the complete velocity vector.

In [13] Kirscht proposed an approach to the moving target detection and velocity estimation based on a sequence of single-look SAR images generated from conventional single-channel SAR. These images are processed using different look center frequencies, therefore showing the ground at different look angles and at different ranges. The cross-range velocity component is obtained from the moving target displacements estimated between successive single-look SAR images. The slant-range velocity component is estimated by evaluating the variation of the signal amplitude during the sequence. This approach relies on thorough measurements of the moving target position and amplitude. This requirement is hard to fulfill, as moving targets appear defocused and/or split when focused with wrong velocity parameters.

This work was supported by the Fundação para a Ciência e Tecnologia, under the project POSI/34071/CPS/2000.

Besides the blind angle ambiguity, the detection and parameter estimation of slowly moving targets or targets with velocity parallel to the radar velocity is another difficulty for single-antenna based systems. The reason is the totally, or almost totally, overlapping between the moving target spectra and the clutter spectrum. The utilization of more than one receiving antenna exploiting multi-channel and space-time-frequency processing schemes (see [14], [15], [16] for an introduction to space-time processing in radar) have been proposed as a way to overcome the limitation of single-antenna based methods. Examples are the multichannel SAR [6], [17], the linear antenna array or velocity SAR (VSAR) [18], the dual-speed SAR [19], and the multifrequency antenna array SAR (MF-SAR) [20]. Each one of these methods yields better results than the single-channel approaches at the expense of higher complexity in the respective hardware and software.

This article, which elaborates on ideas presented in [21], has two main goals. Our first goal consists in showing that, in stripmap SAR, it is possible to infer the complete parameter vector of constant velocity targets using a single sensor; therefore, the azimuth position uncertainty is solved with just a single sensor. The second goal is the derivation of a detector and an estimator for the moving target parameters (i.e., initial coordinates, velocity, and reflectivity). Basically, we exploit the structure of the amplitude and phase modulations of the returned echo from a moving target in the Fourier domain. The echo amplitude is a scaled and shifted replica of the antenna radiation pattern; the scale and shift are functions of slant-range and cross-range velocities, respectively. The echo phase is a function of the moving target velocity magnitude and the target coordinates. A generalized likelihood ratio test is then derived to detect moving targets and to estimate their trajectory parameters.

A crucial step in the detection/estimation scheme is a matched filtering operation, depending on the moving target parameters, that simultaneously copes with range migration and compresses two-dimensional signatures into one-dimensional ones without degrading the slant-range resolution. This matched filtering operation introduces, therefore, a huge simplification on the detector/estimator structure.

The proposed technique yields good results, even for very low signal to clutter ratios (SCRs), whenever the moving target spectra are not totally overlapped with the clutter spectrum. Otherwise, the detector and the estimator still work provided that, roughly, SCR> 10 dB.

The article is organized as follows. In Section II aspects of SAR signals are reviewed, the 2D Fourier transform of the echo from point moving targets is derived, the compressed signals using approximate moving target parameters are characterized, aspects of cross-range sampling are addressed, and, finally, the background and noise statistics are derived. In Section III, a generalized likelihood ratio test is derived to detect moving targets and estimate their trajectory parameters. The detection/estimation problem is formalized as one of detection and parameter estimation of deterministic signals immersed in Gaussian noise. Still in Section III, an efficient scheme to compute the generalized likelihood ratio test is proposed. Section IV presents results illustrating the effectiveness of the proposed methodology.

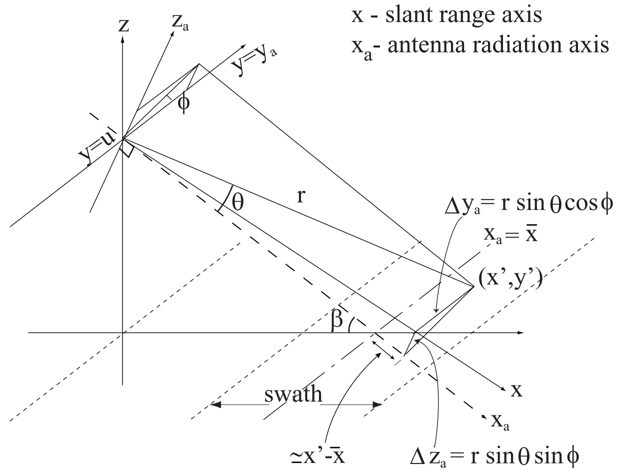

Fig. 2. Antenna aperture in the plane $x_a = 0$, at cross-range $y = u$, moving at constant altitude in the cross-range direction, and illuminating a moving target with slant-plane coordinates $(x = x', y = y')$.

II. Background

FIGURE 2 shows a SAR antenna at cross-range position $y = v_r t \equiv u$, travelling at speed v_r in the cross-range direction and operating at frequency ω_0. The antenna illuminates a single moving target with constant velocity $(-v_x, -v_y)$ in the slant-plane[1], complex reflectivity f, and slant-plane coordinates

$$\begin{cases} x' = x_0 - v_x t = x_0 - \mu u \\ y' = y_0 - v_y t = y_0 - bu, \end{cases}$$

where $(\mu, b) \equiv (v_x/v_r, v_y/v_r)$ is the target relative velocity vector. It is assumed that the moving target and the background, made of static targets, have been spotlighted (see, e.g., [5]) such that the target region is confined to $(x, y) \in [x_m, x_M] \times [y_m, y_M]$, as illustrated in Fig. 1.

The auxiliary coordinate system (x_a, y_a, z_a) and the associated spherical coordinates (r, θ, ϕ) are used to describe the antenna radiation pattern produced by an aperture travelling in the plane $x_a = 0$ at constant cross-range velocity and constant altitude. The reflectivity of the moving target is taken to be independent of the aspect angle[2] and $a(\theta, \phi, \omega)$ is denoted as the two-way antenna radiation pattern at frequency $\omega + \omega_0$.

When the radar is positioned at coordinate $y = u$, the distance between the target and the radar is

$$r \equiv \sqrt{(x_0 - \mu u)^2 + [y_0 - (1 + b)u]^2}. \qquad (1)$$

[1] The minus sign has been adopted as it introduces symmetry in the formalism.

[2] Most man-made targets exhibit reflectivity depending on the aspect angle. However, this assumption greatly simplifies the formulation and yet leads to good results, as shown in Section IV.

Since the system is linear, the output to the pulse $p(t)$ transmitted when the radar is at $y = u$ is, in complex envelope notation,

$$s(u,t) = \frac{1}{2\pi}\int_{-\infty}^{+\infty} \underbrace{a(\phi,\theta,\omega)P(\omega)fe^{-j2kr}}_{s(u,\omega)} e^{j\omega t}d\omega, \qquad (2)$$

where $P(\omega)$ is the Fourier transform of the complex envelope of $p(t)$, $k = 2\pi/\lambda = (\omega+\omega_0)/c$ is the wavenumber (λ is the wavelength at frequency $\omega+\omega_0$), and $s(u,\omega)$ (see footnote[3]) is the Fourier transform of $s(u,t)$ with respect to t. Herein, we follow Soumekh's terminology (see [7, ch. 6.7]), according to which, coordinates u and t are termed *slow-time* domain and *fast-time* domain, respectively. This terminology stems from the fact that the motion of the radar platform is much slower than the speed of light at which the transmitted and backscattered pulses propagate.

Distance r can be written in a more compact form. Expanding the square-root arguments of (1) and denoting $\nu \equiv 1 + b$, we conclude that

$$r = \sqrt{X^2 + (Y-\alpha u)^2}, \qquad (3)$$

where

$$\begin{aligned} X^2 + Y^2 &= x_0^2 + y_0^2, & (4)\\ \alpha Y &= \mu x_0 + \nu y_0, & (5)\\ \alpha &= \sqrt{\mu^2+\nu^2}. & (6) \end{aligned}$$

Still following Soumekh's terminology (see [7, ch. 6.7]), (X,Y) are the *motion-transformed coordinates*, $\sqrt{X^2+Y^2}$ is the *radial range*, αY is the *squint cross-range*, and α is the *relative speed*. Solving equations (4), (5), and (6) with respect to (x_0, y_0), we obtain

$$\begin{bmatrix} x_0 \\ y_0 \end{bmatrix} = \frac{1}{\alpha}\begin{bmatrix} \nu & -\mu \\ \mu & \nu \end{bmatrix}\begin{bmatrix} X \\ Y \end{bmatrix}.$$

The motion-transformed coordinates (X,Y) are a rotation of coordinates (x_0, y_0) by the angle $\arctan(\mu/\nu)$.

The mapping from (x_0, y_0, μ, ν) to (X, Y, α) is not one to one; therefore, assuming that vector (X, Y, α) is known, we can not determine the complete moving target vector (x_0, y_0, μ, ν). The blind angle ambiguity refers to the fact that equations (4), (5), and (6) do not allow us to determine the directions of vectors (μ,ν) and (x_0, y_0), but only their norm [equations (4) and (6), respectively] and the angle between them: notice that αY given by (5) is the inner product between (μ,ν) and (x_0, y_0).

The received echo from a moving target can now be written in the (X, Y, α) domain as

$$s(u,\omega) = a(\theta,\phi,\omega)P(w)fe^{-j2k\sqrt{X^2+(Y-\alpha u)^2}}.$$

Let

$$S(k_u,\omega) \equiv \mathcal{F}_{(u)}\left[s(u,\omega)\right] \qquad (7)$$

be the slow-time Fourier transform of $s(u,\omega)$. To compute (7) we use the stationary phase method (see, e.g., [22]), noting that $a\left[\theta(u),\phi(u),\omega\right]$ is a smooth function of u compared with term $e^{-2jkr(u)}$. Under these circumstances we get

$$S(k_u,\omega) = A(k_u,\omega)P(\omega)fe^{-j\psi(k_u,\omega)}, \qquad (8)$$

where

$$\begin{aligned} A(k_u,\omega) &\propto a(\theta(u),\phi(u),\omega), & (9)\\ \psi(k_u,\omega) &= 2kr(u) + k_u u, & (10) \end{aligned}$$

both (9) and (10) computed at $u = u(k_u)$ such that $\frac{d\psi}{du} = 0$, leading to

$$k_u = -2k\frac{d\psi}{du} = \frac{2k(Y-\alpha u)\alpha}{\sqrt{X^2+(Y-\alpha u)^2}}. \qquad (11)$$

In classical SAR jargon, k_u is termed *slow-time* Doppler domain.

By solving (11) with respect to u (see, e.g., [10]), we get

$$\psi(k_u,\omega) = \sqrt{4k^2 - \left(\frac{k_u}{\alpha}\right)^2} X + \left(\frac{k_u}{\alpha}\right) Y, \qquad (12)$$

valid for $k_u/\alpha \in [-2k, 2k]$. According to (12), phase ψ varies linearly with X and Y. This characteristic is the key element in the Fourier type approach to SAR imaging.

A. Antenna Radiation Pattern

Let us now concentrate on the antenna radiation pattern $A(k_u,\omega)$. Soumekh in [7, ch. 6.7], based on the Fourier decomposition of a spherical wave, derives a formula for $A(k_u,\omega)$ valid for static targets. Herein we present a different approach to compute $A(k_u,\omega)$ valid for constant velocity moving targets.

The two-way antenna radiation pattern from a planar aperture illuminated with constant polarization is [23]

$$a(\theta,\phi,\omega) \propto g^2(k\sin\theta\cos\phi, k\sin\theta\sin\phi), \qquad (13)$$

where $g(k_{y_a}, k_{z_a})$ is the Fourier transform of the electrical field in the antenna aperture. When the polarization over the aperture varies, the relation (13) still holds, but g is more complex.

From Fig. 2 we see that

$$\begin{aligned} k_{y_a} &\equiv k\sin\theta\cos\phi = k\frac{\Delta y_a}{r} = k\frac{y_0-\nu u}{r} & (14)\\ k_{z_a} &\equiv k\sin\theta\sin\phi = k\frac{\Delta z_a}{r} = k\frac{x_0-\mu u-\bar{x}}{r}\tan\beta. & (15) \end{aligned}$$

On the other hand, replacing αY and α^2, given respectively by (5) and (6), into (11) we obtain, after some manipulation,

$$k_u = 2k\mu\frac{x_0-\mu u}{r} + 2k\nu\frac{y_0-\nu u}{r}. \qquad (16)$$

From (1) and (14), we have

$$\frac{x_0-\mu u}{r} = \sqrt{1-\left(\frac{k_{y_a}}{k}\right)^2}. \qquad (17)$$

[3] Although this notation is not strictly correct, since we are defining a function based on its arguments, we have adopted it for better clarity.

Introducing (17) and (14) into (16), we obtain

$$k_u = 2k\mu\sqrt{1-\left(\frac{k_{y_a}}{k}\right)^2} + 2\nu k_{y_a}. \tag{18}$$

Equation (18) can be converted into a $2nd$ order polynomial and solved with respect to k_{y_a}. We note however that $\sqrt{1-(k_{y_a}/k)^2} \simeq 1-(\sin\theta\cos\phi)^2/2$. If the antenna beamwidth is smaller than, say, $10°$, then $(\sin\theta\cos\phi)^2/2 < 4\times 10^{-3}$. Therefore $\sqrt{1-(k_{y_a}/k)^2} \simeq 1$ is a good approximation for most SAR applications. We then have

$$\begin{aligned} k_{y_a} &\approx \frac{1}{2\nu}[k_u - 2k\mu] & (19)\\ k_{z_a} &\approx k\left(1-\frac{\bar{x}}{r'}\right)\tan\beta, & (20)\end{aligned}$$

where r' denotes the range corresponding to the middle of the integration interval. The expression for k_{z_a} was obtained by replacing (17) into (15) and again noting that $\sqrt{1-(k_{y_a}/k)^2} \simeq 1$.

The spatial frequency k_{z_a} depends on the wavenumber k and on the target range r'. If $x_M - x_m$, the length of the target area in slant-range, is much smaller than $\bar{x}$, then $\bar{x}/r' \simeq 1$ and we have

$$A(k_u,\omega) \propto g^2\left[\frac{1}{2\nu}(k_u-2k\mu),0\right], \tag{21}$$

i.e., the range dependence of $A(k_u,\omega)$ can be neglected. If $x_M - x_m$ is not much smaller than $\bar{x}$, then the antenna radiation pattern becomes dependent on the range r'. However, this dependency can be removed by introducing a proper slant-range dependent gain. From now on we assume that the antenna radiation pattern does not depend on r'.

In deriving $A(k_u,\omega)$, we have assumed that the antenna has broadside geometry, i.e., the antenna radiation axis is orthogonal to the azimuthal direction. However, there are situations, for example due to wind drift, in which the antenna displays squinted geometries. In order to include general geometries in the echo amplitude $A(k_u,\omega)$, let us assume that the antenna aperture shown in Fig. 2 has been rotated by an angle θ_0 with respect to axis z_a such that the rotated radiation axis has coordinates $\theta=\theta_0$ and $\phi=0$. Notice that the antenna radiation pattern $A(k_u,\omega)$ given by (21) is parameterized only by the relative velocity vector (μ,ν) measured in the slant-plane defined by the coordinates y_a and x_a. Therefore, the antenna radiation pattern for a squinted geometry is given by

$$A(k_u,\omega) \propto g^2\left[\frac{1}{2\nu_s}(k_u-2k\mu_s),0\right], \tag{22}$$

where (μ_s,ν_s) is the relative velocity vector (μ,ν) expressed in the coordinates y_a and x_a rotated by θ_0; i.e.,

$$\begin{bmatrix}\mu_s\\ \nu_s\end{bmatrix} = \begin{bmatrix}\cos\theta_0 & \sin\theta_0\\ -\sin\theta_0 & \cos\theta_0\end{bmatrix}\begin{bmatrix}\mu\\ \nu\end{bmatrix}.$$

The shift $k_{DC} \equiv 2k\mu_s$ is commonly termed the Doppler centroid.

Concluding, the illumination function in the slow-time Doppler domain, k_u, takes the shape of the antenna radiation pattern with respect to k_{y_a}. The shape becomes expanded by factor $2\nu_s$ and shifted by $2k\mu_s$. For broadside antenna geometry (i.e., $\theta_0=0$) the expansion is given by $2k\nu$ (i.e., depends only on the cross-range relative velocity) and the shift is given by $2k\mu$ (i.e., depends only on the slant-range relative velocity).

The remainder of the paper is devoted to building a detector of moving targets and an estimator of their parameters (μ_s,ν_s,X,Y), both based on the structure of the received signal $S(k_u,\omega) = A(k_u,\omega)P(\omega)e^{-\psi(k_u,\omega)}$. Notice that the phase $\psi(k_u,\omega)$ is informative with respect to α, X, and Y, whereas $A(k_u,\omega)$ is informative with respect to μ_s and ν_s. Once these parameters have been inferred, we solve equations (4), (5), and (6) to determine the moving target parameters (μ_s,ν_s,x_0,y_0). The azimuth ambiguity is therefore solved using a single sensor.

The proposed method when applied to background targets without internal motion yields the Doppler centroid of these targets. This parameter is of prime importance in SAR imaging. Furthermore, and given that the relative velocity vector (μ,ν) of a background target is known beforehand, the squint angle θ_0 can be obtained from the vector (μ_s,ν_s) of a background target using $\theta_0 = \text{angle}(\mu,\nu) - \text{angle}(\mu_s,\nu_s)$. Hence, we assume from now on that $\theta_0=0$.

In the remainder of the paper we assume that the background targets are static (i.e., $\mu=0$ and $\nu=1$). This scenario applies to airborne SAR. However, the concepts and ideas apply to constant velocity moving background targets, as occurs, for example, in spaceborne SAR, due to the earth rotation.

B. Compression of the Moving Target Echo

Let us consider a single moving target with parameters (μ,ν,X,Y,f) and echo S_m immersed in background echo S_0. The total returned echo is given by

$$S(k_u,\omega) = S_m(k_u,\omega) + S_0(k_u,\omega), \tag{23}$$

with

$$\begin{aligned} S_m(k_u,\omega) &= P(\omega)A(k_u)fe^{-j\psi(k_u,\omega)}, & (24)\\ S_0(k_u,\omega) &= P(\omega)A_0(k_u)\sum_n f_n e^{-j\psi_n(k_u,\omega)}, & (25)\end{aligned}$$

where the dependency of A on ω has been omitted, vector $A_0(k_u)$ denotes the amplitude echo of a static target (i.e., $\mu=0,\nu=1$), and phases $\psi(k_u,\omega)$ and $\psi_n(k_u,\omega)$ are given by (12) for the moving target parameters (α,X,Y) and $(1,X_n,Y_n)$, respectively.

According to (24), the moving target echo is spread over the two dimensional domain $(k_u,\omega)\in S_{PA}$, the support[4] of $P(\omega)A(k_u)$, thus introducing complexity in any moving

[4]By support of f, we mean the set of (k_u,ω) points where $f(k_u,\omega)\neq 0$.

target detection/estimation scheme. To compress the moving target echo into a one-dimensional domain, let us define the signal

$$s_c(k_u,t) \equiv \mathcal{F}^{-1}_{(\omega)}\left[S(k_u,\omega)P^*(\omega)e^{j\psi'(k_u,\omega)}\right], \tag{26}$$

where $\psi'(k_u,\omega)$ is given by (12) for moving target parameters $(\alpha', X', 0)$ *close* to $(\alpha, X, 0)$. In appendix A, we show that if $\mu \ll c/(BD_y)$, where c is the speed of light, B the pulse bandwidth, and D_y the cross-range aperture width, and $|X/\alpha^4 - X'/\alpha'^4| \ll (64\pi k_0^3)/|k_u|^4_{max}$, then

$$s_c(k_u,t) = \underbrace{fR_p[t-\tau(k_u)]A(k_u)e^{-j\eta(k_u)}}_{s_{mc}} + w(k_u,t), \tag{27}$$

with

$$\tau(k_u) = \frac{2(X-X')}{c} + \frac{1}{c}\left(\frac{k_u}{2k_0}\right)^2\left(\frac{X}{\alpha^2} - \frac{X'}{\alpha'^2}\right) \tag{28}$$

$$\eta(k_u) = -\frac{k_u^2}{4k_0}\left(\frac{X}{\alpha^2} - \frac{X'}{\alpha'^2}\right) + k_u\frac{Y}{\alpha} + \varphi, \tag{29}$$

where $R_p(t)$ is the deterministic autocorrelation of the transmitted pulse $p(t)$, $\varphi = 2k_0(X - X')$, and $w(k_u,t)$ is the term due to the background echo.

The energy of autocorrelation $R_p(t)$ is highly concentrated about $t = 0$. Therefore, the energy of $s_{mc}(k_u,t)$ is highly concentrated about $t = \tau(k_u)$. For $\alpha'^2 X = \alpha^2 X'$, the delay $\tau(k_u)$ does not depend on k_u, meaning that energy of $s_{mc}(k_u,t)$ is clustered along the cross-range direction. By exploiting this fact, we derive, in the next section, a moving target detector and parameter estimator that simultaneously copes with range migration and straightens the moving target signatures in the (k_u,t) domain along coordinate k_u without degrading the slant-range resolution. For a given X', the estimator scans the set $\alpha \in [\alpha_{min}, \alpha_{max}]$ and detects moving targets with coordinate X in an interval such that $|X/\alpha^4 - X'/\alpha'^4| \ll (64\pi k_0^3)/|k_u|^4_{max}$.

C. Noise statistics

The moving target echo is contaminated by the system noise and by the background echo. In order to formulate the moving target detection and estimation problems we are addressing, we need to determine the statistics of both sources.

In appendix B we show that if the number of background scatterers per resolution cell is large, none is predominant, they are mutually independent, and each one has a phase independent of its amplitude, then the random field $w(k_u,t)$ is zero-mean complex Gaussian circular. Assuming that backscattering coefficient σ° is constant within the target area, then the covariance of $w(k_u,t)$ at time t, $C_w(k_{u_1},k_{u_2}) \equiv E\left[s_c(k_{u1},t)s_c^*(k_{u2},t)\right]$, satisfies

$$C_w(k_{u_1},k_{u_2}) = \begin{cases} \beta|A(k_{u_1})|^2 & k_{u_1} = k_{u_2} \\ 0 & k_{u_1} - k_{u_2} = 2l\pi/L, \end{cases} \tag{30}$$

where l is an integer, $\beta \equiv \sigma^\circ L E_{R_p}$, L is the target area cross-range length (see Fig. 1), and E_{R_p} is the energy of the autocorrelation of the transmitted pulse.

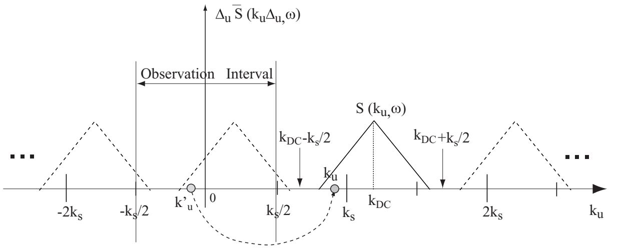

Fig. 3. Illustration of the relation between the discrete Fourier transform of $s(n\Delta_u,\omega)$ with respect to n, $\overline{S}(k_u\Delta_u,\omega)$, and the Fourier transform of $s(u,\omega)$ with respect to u, $S(k_u,\omega)$.

In deriving (30) we have assumed that the background targets have constant velocity and do not display internal motion, such as leaves moving in the wind, or waves in water bodies. We should say, however, that if there is internal motion in the SAR scene, the best approach to determine the covariance $C_w(k_{u_1},k_{u_2})$ is probably to estimate it directly from data, for it depends on the internal motion statistics, which are normally unknown.

Concerning the system noise $n(u,t)$, we assume that it is zero-mean complex Gaussian circular and white. A reasoning similar to that of Appendix B leads to the conclusion that

$$C_n(k_{u_1},k_{u_2}) = \begin{cases} \gamma, & k_{u_1} = k_{u_2} \\ 0, & k_{u_1} - k_{u_2} = 2l\pi/L. \end{cases} \tag{31}$$

where l is an integer and $\gamma \equiv \sigma^n L E_p$, with σ^n being the noise spectral power and E_p the energy of $p(t)$. Note that γ is proportional to E_p, whereas β is proportional to E_{R_p}. The reason is that $w(u,t)$ is filtered by the filter $|P(\omega)|^2$, whereas $n(u,t)$ is filtered with filter $P^*(\omega)$.

Under the assumption of constant reflectivity σ° along the cross-range dimension, the background noise plus the system noise satisfies

$$C_w(k_{u_1},k_{u_2}) \approx \begin{cases} \beta|A(k_{u_1})|^2 + \gamma, & k_{u_1} = k_{u_2} \\ 0, & k_{u_1} - k_{u_2} = 2l\pi/L. \end{cases} \tag{32}$$

D. Cross-range Sampling

From (13) and (21), and noting that the aperture radiated field is confined to $|\theta| \leq \theta_M \ll 1$ and $|\phi| \ll 1$, we conclude that the support of $s_{mc}(k_u,t)$ with respect to k_u is $k_u \in [-2\nu k\theta_M + k_{DC}, 2\nu k\theta_M + k_{DC}]$. The antenna beamwidth $2\theta_M$ depends on the aperture illumination. Using the indicative value $\theta_M = \lambda/(2D_y)$ (D_y denotes the cross-range aperture width), we have $k_u \in [-2\nu\pi/D_y + k_{DC}, 2\nu\pi/D_y + k_{DC}]$. The bandwidth of $s_{mc}(u,t)$ with respect to u is therefore $4\pi\nu/D_y$. As the SAR system is sampled with respect to the cross-range, then, according to the Nyquist theorem, the cross-range sampling interval must satisfy $\Delta_u \leq D_y/(2\nu)$.

Let $\bar{S}(\Omega,\omega)$ be the discrete Fourier Transform of sequence $s(n\Delta_u,\omega)$ with respect to the integer variable n. The function $\Delta_u\bar{S}(k_u\Delta u,\omega)$ is a periodic extension of $S(k_u,\omega)$ of period $k_s \equiv 2\pi/\Delta_u$. Since the sampling frequency k_s is above the Nyquist rate, the successive replicas of $S(k_u,\omega)$ do not overlap. This is illustrated in Fig. (3), which shows spectra $\Delta_u\bar{S}(k_u\Delta u,\omega)$ and $S(k_u,\omega)$.

To obtain the compressed moving target echo (26) we should then compute

$$s_c(k_u,t)\equiv \mathcal{F}^{-1}_{(\omega)}\left[\Delta_u\bar{S}(k_u\Delta_u,\omega)P^*(\omega)e^{j\psi'(k_u,\omega)}\right], \quad (33)$$

for $k_u\in[k_{DC}-k_s/2,k_{DC}+k_s/2[$. In practice, the discrete Fourier transform $\bar{S}(\Omega,\omega)$ is computed by the fast Fourier transform (FFT) algorithm at a set of equispaced discrete frequencies $k_u\in[-k_s/2,k_s/2[$ (observation interval in Fig. (3)). These frequencies should be mapped onto the interval $[k_{DC}-k_s/2,k_{DC}+k_s/2[$, as it is indicated by an arrow in Fig. (3) linking k_s' to k_s. Note that, for a given Doppler centroid k_{DC}, the couple (k_u,k_u') is unique and satisfies

$$k_u=qk_s+k_u', \qquad k_u\in[k_{DC}-k_s/2,k_{DC}+k_s/2[, \quad (34)$$

where q is an integer. The Doppler centroid dependent mapping (34) between k_u and k_u' plays an important role in the algorithms presented in the next section.

III. Detection/estimation problem

Suppose that we have identified a pair (X',α') such that the quadratic phase term in expression (28) is neglegible in comparison with the fast-time range resolution. In this case, the signal $s_{mc}(k_u,t)$ has been straightened along $\tau=(2/c)(X-X')$. Furthermore, assuming that we measure τ, then the motion transformed coordinate X and the relative speed α are approximately given by $X\simeq X'+(c/2)\tau$ and $\alpha\simeq\alpha'\sqrt{X/X'}$.

Define

$$\begin{aligned}\mathbf{s} &\equiv [s_{-N},\dots,s_0,\dots,s_{N-1}]^T \quad (35)\\ \mathbf{a} &\equiv [a_{-N},\dots a_0,\dots,a_{N-1}]^T,\end{aligned}$$

where

$$\begin{aligned}s_i &= s_c(k_{u_i},\tau)e^{j\frac{k_{u_i}^2}{4k_0}\frac{X'}{\alpha'^2}}\\ a_i &= A(k_{u_i})e^{j\frac{k_{u_i}^2}{4k_0}\frac{X}{\alpha^2}}e^{-j\frac{k_{u_i}Y}{\alpha}},\end{aligned}$$

with $k_{u_i}=k_{u_0}+(2\pi i)/L$ for $i=-N,\dots,0,\dots,N-1$, $N=\lceil Lk_s/(4\pi)\rceil$ ($\lceil x\rceil$ denotes the smallest integer larger than or equal to x), and k_{u_0} the multiple of $(2\pi)/L$ closest to k_{DC}. Since the fast Fourier transform (FFT) is used to compute the discrete time Fourier transform, then using $2N$ points in the k_u domain implies using $2N$ points in the u domain to sample the cross-range length L . Therefore, with this setting, the cross-range sampling interval is $\Delta_u=L/(2N)\le(2\pi)/k_s$, thus satisfying the Nyquist limit.

For a given moving target parameters vector $\boldsymbol{\theta}\equiv(\mu,\nu,X,Y)$ and reflectivity f, the density of vector $\mathbf{s}$ is

$$p(\mathbf{s}|f,\boldsymbol{\theta})=\mathcal{N}(\boldsymbol{\mu}_s,\mathbf{C}_s), \quad (36)$$

where the mean $\boldsymbol{\mu}_s\equiv E[\mathbf{s}]$ and the covariance $\mathbf{C}_s\equiv E[(\mathbf{s}-\boldsymbol{\mu}_s)(\mathbf{s}-\boldsymbol{\mu}_s)^H]$ are, according to (27) and (32) and assuming that $R_p(0)=1$, given by

$$\begin{aligned}\boldsymbol{\mu}_s &= f\mathbf{a}(\boldsymbol{\theta})\\ \mathbf{C}_s &= \operatorname{diag}\left(\beta|\widetilde{A}_0(k_{u_i})|^2+\gamma\right),\ \ i=-N,\cdots,N-1,\end{aligned}$$

where the operator $\widetilde{h}(k_u)$ denotes a k_s-periodic extension of $h(k_u)$.

The problem at hand is a binary test: under the hypothesis $\mathcal{H}_0$, the received signal is the background echo; under the alternative hypothesis $\mathcal{H}_1$, the received signal is the background echo plus the moving target echo, i.e.,

$$\begin{aligned}\mathcal{H}_0: &\quad \mathbf{s}=\mathbf{w}\\ \mathcal{H}_1: &\quad \mathbf{s}=f\mathbf{a}(\boldsymbol{\theta})+\mathbf{w}, \quad (37)\end{aligned}$$

where $\mathbf{w}\equiv[w_{-N}\cdots w_0\cdots w_{N-1}]^T$, with $w_i\equiv\widetilde{w}(k_{u_i},\tau)$, for $i=-N,...,0,...,N-1$.

We adopt the *generalized likelihood ratio test* (GLRT) [24] to our detection problem, which, in the present case, amounts to computing the test

$$l(\mathbf{s})\underset{\mathcal{H}_0}{\overset{\mathcal{H}_1}{\gtrless}}\eta, \quad (38)$$

with η being the detection threshold and

$$l(\mathbf{s})\equiv\ln\left\{\frac{p(\mathbf{s}|\widehat{f},\widehat{\boldsymbol{\theta}})}{p(\mathbf{s}|f=0)}\right\}, \quad (39)$$

where the maximum likelihood estimates $(\widehat{f},\widehat{\boldsymbol{\theta}})$ are given by

$$(\widehat{f},\widehat{\boldsymbol{\theta}})=\arg\max_{f,\boldsymbol{\theta}}\left\{-[\mathbf{s}-f\mathbf{a}(\boldsymbol{\theta}))]^H\mathbf{C}_s^{-1}[\mathbf{s}-f\mathbf{a}(\boldsymbol{\theta})]\right\}, \quad (40)$$

and $p(\mathbf{s}|f=0)$ is the density of noise $\mathbf{w}$.

To achieve a compact notation, we introduce the inner product $\langle\mathbf{x},\mathbf{y}\rangle\equiv\sum_{i=-N}^{N-1}x_ic_i^{-1}y_i^*$ and the induced norm $\|\mathbf{x}\|^2\equiv\langle\mathbf{x},\mathbf{x}\rangle$, where $\mathbf{x},\mathbf{y}\in C^{2N}$ (C denotes the complex set) and $c_i\equiv[\mathbf{C}_s]_{ii}$.

Noting that the distance $\|\mathbf{s}-f\mathbf{a}\|$ is minimized when $\langle\mathbf{s}-f\mathbf{a},\mathbf{a}\rangle=0$ (i.e., the error $\mathbf{s}-f\mathbf{a}$ is orthogonal to $\mathbf{a}$) and after some algebra we obtain

$$\begin{aligned}\widehat{f} &= \frac{\langle\mathbf{s},\widehat{\mathbf{a}}\rangle}{\|\widehat{\mathbf{a}}\|^2} \quad (41)\\ \widehat{\boldsymbol{\theta}} &= \arg\max_{\boldsymbol{\theta}}\left\{\frac{|\langle\mathbf{s},\mathbf{a}(\boldsymbol{\theta})\rangle|^2}{\|\mathbf{a}(\boldsymbol{\theta})\|^2}\right\} \quad (42)\\ l(\mathbf{s}) &= \frac{|\langle\mathbf{s},\widehat{\mathbf{a}}\rangle|^2}{\|\widehat{\mathbf{a}}\|^2}, \quad (43)\end{aligned}$$

where $\widehat{\mathbf{a}}\equiv\mathbf{a}(\widehat{\boldsymbol{\theta}})$.

Since $\langle\mathbf{s},\mathbf{a}\rangle=\|\mathbf{a}\|\,\|\mathbf{s}\|\cos\alpha_{\mathbf{as}}$, where $\alpha_{\mathbf{as}}$ is the angle between vectors $\mathbf{a}$ and $\mathbf{s}$, the maximum likelihood estimator of $\boldsymbol{\theta}$ seeks the estimate $\widehat{\mathbf{a}}$ with highest angular proximity to observed data $\mathbf{s}$. Moreover, the inner products present in (42) implements noise plus clutter suppression by attenuating vectors $\mathbf{a}(\boldsymbol{\theta})$ and $\mathbf{s}$ proportionally to noise plus clutter power $\beta|\widetilde{A}_0(k_{u_i})|^2+\gamma$.

We adopt the Neyman-Pearson approach to signal detection. Therefore, the threshold η that maximizes the *probability of detection* $P_D=\{\mathbf{s}:l(\mathbf{s})>\eta\,|\,\mathcal{H}_1\}$ is found from the *false alarm probability* $P_{FA}=\{\mathbf{s}:l(\mathbf{s})>\eta\,|\,\mathcal{H}_0\}$. Explicit expressions for densities $p(l|\mathcal{H}_0)$ and $p(l|\mathcal{H}_1)$ are not available because $\widehat{\mathbf{a}}$ is an unknown nonlinear function of random vector $\mathbf{s}$. In order to obtain approximate values of η and to derive bounds for the detector performance, we assume for a while that the detector has perfect knowledge of the parameter $\mathbf{a}$ (this is the so-called *clairvoyant detector* [24]). In this case, the probability of $\langle \mathbf{s}, \mathbf{a}\rangle$ is $\mathcal{N}(0, \|\mathbf{a}\|^2)$ under hypothesis H_0 and $\mathcal{N}(f\|\mathbf{a}\|^2, \|\mathbf{a}\|^2)$ under hypothesis H_1. Thus, the density of $2l$ is

$$2l \sim \begin{cases} \chi_2^2 & \text{under } \mathcal{H}_0 \\ \chi_2'^2(|f|^2\|\mathbf{a}\|^2) & \text{under } \mathcal{H}_1, \end{cases}$$

where χ_2^2 denotes the *chi-squared* density with 2 degrees of freedom and $\chi_2'^2(\lambda)$ denotes the *noncentral chi-squared* density with 2 degrees of freedom and noncentrality parameter λ. Since density χ_2^2 is the exponential density of mean 2, the threshold η is then given by

$$\eta = -\ln P_{FA}.$$

The detector performance depends only on the noncentrality parameter

$$\begin{aligned} |f|^2\|\mathbf{a}\|^2 &= \sum_{i=-N}^{N-1} \frac{|f|^2 E_p^2 |A(k_{u_i})|^2}{\beta|\widetilde{A}_0(k_{u_i})|^2 + \gamma} \qquad (44) \\ &\simeq \frac{1}{2\pi}\int_{\frac{-k_s}{2}}^{\frac{-k_s}{2}} \frac{|f|^2 E_p^2 |\widetilde{A}(k_u)|^2}{\sigma^0 E_{R_p}|\widetilde{A}_0(k_u)|^2 + \sigma^n E_p}\, dk_u. \end{aligned}$$

The expression on the right hand side of (44) is the best signal to clutter plus noise ratio (SCNR$_{opt}$) that it is possible to attain, which is achieved by compressing the signal plus clutter noise signature (27) with the matched filter $A^\star(k_u)/(\sigma^0 E_{R_p}|\widetilde{A}_0(k_u)|^2 + \sigma^n E_p)$ (see, e.g., [25] for the derivation of the matched filter).

For a given backscattering coefficient σ^0 and noise spectral power σ^n, the SCNR$_{opt}$ depends on the antenna radiation pattern $A(k_u)$ through the relative velocities μ and ν. Assuming a large clutter to noise ratio (CNR), then the function $1/(\sigma^0 E_{R_p}|\widetilde{A}_0(k_u)|^2 + \sigma^n E_p)$ exhibits a high-pass shape with cut-band roughly corresponding to the support of $A_0(k_u)$. Therefore, the lowest values of SCNR$_{opt}$ correspond to antenna radiation patterns $A(k_u)$ whose support are totally contained in the support of $A_0(k_u)$. If the support of $A(k_u)$ becomes a little displaced with respect to the support of $A_0(k_u)$, then part of $A(k_u)$ is amplified by the high-pass filter and the SCNR$_{opt}$ becomes large, thus increasing the probability of detection. As a conclusion, the targets most hard to detect are those with cross-range velocity parallel to the platform motion (i.e., $\nu \leq 1$) and slant-range relative velocities multiple of $k_s/(2k_0)$.

Fig. 4 plots the detection performance of the Neyman-Pearson detector, assuming perfect knowledge of the moving target parameters (μ, ν, X, Y). As an indication of the detector performance, we have $P_D > 0.8$ for SCNR$_{opt} \gtrsim 10$ and $P_{F_A} = 10^{-2}$. The detection probability of the realizable detector is, of course, below the bounds plotted in Fig. 4.

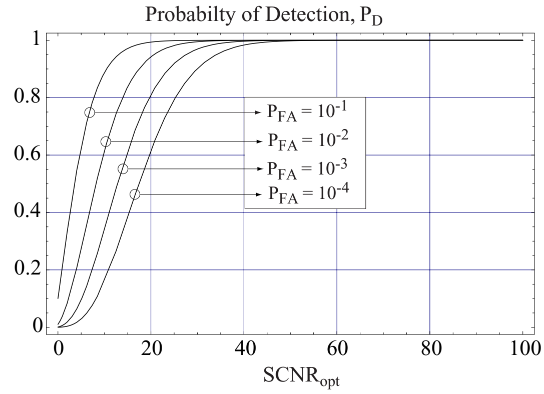

Fig. 4. Detection performance of the Neyman-Pearson detector, assuming perfect knowledge of the moving target parameters.

According to the rationale just presented, the SCNR$_{opt}$ is the most important figure concerning detection performance in SAR. Nevertheless, most authors when referring to SCNR do not have SCNR$_{opt}$ in mind. This is a source of confusion, as the SCNR depends on the compression filter. In this paper and for comparison purposes, when referring to SCNR, we are assuming a flat compression filter. We then have

$$\text{SCNR} \simeq \frac{1}{2\pi}\frac{\left| f_m E_p \int_{\frac{-k_s}{2}}^{\frac{-k_s}{2}} \widetilde{A}(k_u)\, dk_u \right|^2}{\int_{\frac{-k_s}{2}}^{\frac{-k_s}{2}} \left(\sigma^0 E_{R_p}|\widetilde{A}_0(k_u)|^2 + \sigma^n E_p\right)\, dk_u}. \qquad (45)$$

The SCNR, as given by (45), does not depend on the slant-range relative velocity μ. The same is not true concerning SCNR$_{opt}$, as we have discussed above: assuming a high CNR, even a small μ leads to a high SCNR$_{opt}$.

A. Moving Target Parameters Estimation Algorithm

Computing the maximum likelihood estimate (42) amounts to a multidimensional nonlinear optimization of the unknown parameters $(\mu, \nu, X, Y) \in \mathbb{R}^4$, with unbearable computational burden. Herein, instead of computing the exact maximizer of $l(\mathbf{s}, \boldsymbol{\theta}) \equiv |\langle \mathbf{s}, \mathbf{a}(\boldsymbol{\theta})\rangle|^2/\|\mathbf{a}(\boldsymbol{\theta})\|^2$, we adopt a suboptimal approach that iteratively maximizes $l(\mathbf{s}, \boldsymbol{\theta})$ on given subsets of $\mathbb{R}^4$. First we assume that there are available rough estimates of X, α, and k_{DC}; the first two estimates allow getting vector $\mathbf{s}$ from the compressed signal $s_c(k_u, t)$ and the former estimate determines the interval $[\widehat{k}_{DC} - k_s/2, \widehat{k}_{DC} + k_s/2[$ containing the support of $S_m(k_u, \omega)$, with respect to k_u. At the end of this section we present an algorithm to compute these estimates.

Let us denote

$$l(\mathbf{s}, \mu, \nu) \equiv \arg\max_Y l(\mathbf{s}, \mu, \nu, Y). \qquad (46)$$

Parameter X has been omitted as we are assuming that it is known. The dependency of $l(\mathbf{s}, \boldsymbol{\theta})$ on Y is only through the term $|\langle \mathbf{a}, \mathbf{s} \rangle|$, which can be expanded as

$$|\langle \mathbf{a}, \mathbf{s} \rangle| \quad = \quad \left| \sum_{i=-N}^{N-1} b_i e^{-j\Omega i} \right|, \tag{47}$$

where $b_i \equiv A(k_{u_i}) e^{j k_{u_i}^2 X/(4k_0\alpha^2)} c_i^{-1} s_i^*$ and $\Omega \equiv 2\pi Y/(L\alpha)$. Notice that, by using the FFT, $|\langle \mathbf{a}, \mathbf{s} \rangle|$ can be computed efficiently at $\Omega_i = (\pi/N)i$, for $i = -N \ldots, 0, \ldots, N-1$. The frequency $\widehat{\Omega} = \Omega_i$ corresponding to the maximum of $|\langle \mathbf{a}, \mathbf{s} \rangle|$ leads to $\widehat{Y} = \alpha L \widehat{\Omega}/(2\pi)$. The absolute error of $\widehat{Y}$ due to the discrete nature of the FFT is $\alpha L/(4N) \simeq \alpha \Delta_u/2$.

Algorithm 1 Determines moving target parameters (μ, ν, Y) of a single moving target and solves azimuth position uncertainty.

Input: $\widehat{X}, \widehat{\alpha}^{(0)}, \widehat{k}_{DC}, S(k_u, \omega)$
Output: $\widehat{\mu}, \widehat{\nu}, \widehat{Y}, \widehat{x}_0, \widehat{y}_0$
Set: t_{max}
1: $\mathbf{s} := \mathbf{s}\left(\widehat{\alpha}^{(0)}, \widehat{X}, \widehat{k}_{DC}\right)$ {Expressions (33) and (35)}
2: **for** $t := 1$ to $t := t_{max}$ **do**
3: $\left(\widehat{\mu}^{(t)}, \widehat{\nu}^{(t)}\right) := \arg \max_{\substack{\mu,\nu \\ \mu^2+\nu^2=\left(\widehat{\alpha}^{(t-1)}\right)^2}} l(\mathbf{s}, \mu, \nu)$
4: $\widehat{\nu}^{(t)} := \arg\max_{\nu} l(\mathbf{s}, \widehat{\mu}^{(t)}, \nu)$
5: $\widehat{\alpha}^{(t)} := \sqrt{\left(\widehat{\mu}^{(t)}\right)^2 + \left(\widehat{\nu}^{(t)}\right)^2}$
6: **end for**
7: $\widehat{Y} := \widehat{\alpha} L \widehat{\Omega}/(2\pi)$
8: $\widehat{x}_0 := (\widehat{\nu}\widehat{X} + \widehat{\mu}\widehat{Y})/\widehat{\alpha}$
9: $\widehat{y}_0 := (\widehat{\nu}\widehat{Y} - \widehat{\mu}\widehat{X})/\widehat{\alpha}$ {Solve azimuth ambiguity}

Algorithm 1 shows the pseudo-code to determine $(\widehat{\mu}, \widehat{\nu}, \widehat{Y})$ and to solve the azimuth position uncertainty. Step 1 implements the fast-time compression (33) and selects vector $\mathbf{s}$ given by (35). Steps 3 and 4 implement one-dimensional searches and were designed to minimize the parameter search space: step 3 maximizes $l(\mathbf{s}, \mu, \nu)$ over the circle $\mu^2 + \nu^2 = \left(\widehat{\alpha}^{(t-1)}\right)^2$; step 4 maximizes $l(\mathbf{s}, \mu, \nu)$ over the line $\mu = \widehat{\mu}^{(t)}$.

Algorithm 2 implements step 3 of Algorithm 1 by means of a discrete search with $2M_\mu + 1$ equi-spaced points in the interval $\mu \in [\mu_c - \Delta\mu_{max}, \mu_c - \Delta\mu_{max}]$, keeping $\alpha = \widehat{\alpha}^{(t-1)}$. Relative velocities μ_c and $\Delta\mu_{max}$ correspond to the Doppler frequency $\widehat{k}_{DC}$ and to half of sampling frequency k_s, respectively.

Algorithm 3 implements step 4 of Algorithm 1 by means of a discrete search with $2M_\nu + 1$ equi-spaced points in the interval $\nu \in [\widehat{\nu}^{(t)} - \Delta\nu_{max}, \widehat{\nu}^{(t)} + \Delta\nu_{max}]$, keeping $\mu = \widehat{\mu}^{(t)}$.

The unidimensional discrete searches of Algorithms 2 and 3 were designed in a multigrid fashion using ten points per resolution level and three depth levels. This procedure works very well and speeds up the execution time of these algorithms by orders of magnitude.

To determine the input parameters $(\widehat{X}, \widehat{\alpha}^{(0)}, \widehat{k}_{DC})$ for Algorithm 1, we exploit, in Algorithm 4, the fact that

Algorithm 2 Searches for (μ, ν) over a circle (step 3 of Algorithm 1).

Input: $\mathbf{s}$, $\widehat{\alpha}$, $\widehat{k}_{DC}$
Output: $\widehat{\mu}$, $\widehat{\nu}$
Initialization: $\Delta\mu_{max} := k_s/(4k_0)$, $\mu_c := \widehat{k}_{DC}/(2k_0)$
Set: M_μ
1: **for** $i := -M_\mu, \ldots, M_\mu$ **do**
2: $\mu(i) := \mu_c + (i/M_\mu)\Delta\mu_{max}$
3: $\nu(i) := \sqrt{\left(\widehat{\alpha}^{(t-1)}\right)^2 - \mu^2(i)}$
4: $l(i) := l(\mathbf{s}, \mu(i), \nu(i))$ {Expression (43)}
5: **end for**
6: $i := \text{index}\,(\max(l))$
7: $\widehat{\mu}^{(t)} := \mu(i)$, $\widehat{\nu}^{(t)} := \nu(i)$

Algorithm 3 Searches for (μ, ν) over a line (step 4 of Algorithm 1).

Input: $\mathbf{s}$, $\widehat{\mu}^{(t)}$, $\widehat{k}_{DC}$
Output: $\widehat{\nu}$, $\widehat{\Omega}$
Set: $\Delta\nu_{max}$, M_ν
1: **for** $i := -M_\nu, \ldots, M_\nu$ **do**
2: $\nu(i) := \widehat{\nu}^{(t)} + (i/M_\nu)\Delta\nu_{max}$
3: $l(i) := l(\mathbf{s}, \widehat{\mu}^{(t)}, \nu(i))$ {Expression (43)}
4: **end for**
5: $i := \text{index}\,(\max(l))$
6: $\widehat{\nu}^{(t)} := \nu(i)$
7: $\widehat{\Omega} := \Omega(i)$

any triplet X', α', k'_{DC} satisfying $X/\alpha^2 = X'/\alpha'^2$ and $|k_{DC} - k'_{DC}| \le k_s - (4\pi\nu/D_y)$ (recall that $4\pi\nu/D_y$ is the Doppler bandwidth) set to zero the quadratic term of expressions (28) and (29). Hence, we set $X' = \bar{x}$ and scan the parameters α' and k'_{DC}. To test if the quadratic terms of expressions (28) and (29) are close to zero we use the likelihood ratio test applied to each range. The compressed signature (26) is computed (step 5) for each point of the discrete set $\{\alpha_i\}_{i=1}^{M_\alpha} \times \{k_{DC_i}\}_{i=1}^{M_k}$. The sampling interval of the relative speed α is small enough to assure that there is an α_i in the set that straightens the moving target signature along the k_u coordinate in the compressed image $s_c(k_u, t)$.

For each image $s_c(k_u, t)$ compressed with the FFT algorithm using parameters α_j and k_{DC_i}, we compute the likelihood ratio test $l(\mathbf{s}, \mu_i, \nu_j)$, with $\mu_i = k_{DC_i}/(2k_0)$ and $\nu_j = \sqrt{\alpha_j^2 - \mu_i^2}$, for each slant-range $X(n)$ (i.e., $\mathbf{s} := \mathbf{s}(\alpha_j, X(n), k_{DC_i})$, for $n = 1, \ldots, M_x$). Step 17 corrects the estimate of α using the fact that $X/\alpha^2 \simeq X'/\alpha'^2$ when the quadratic terms of expressions (28) and (29) become zero.

Algorithm 4 finds the stronger moving target in the target area. To detect all moving targets, lines 15 to 18 should be replaced in order to find all sets $(\widehat{\alpha}(n), \widehat{k}_{DC}(n), \widehat{X}(n))$, for $n = 1, \ldots, M_x$, such that the likelihood ratio $l(1, n)$ exceeds a given predefined threshold η. This scheme might, however, produce false alarms, since, when the signature

Algorithm 4 Determines parameters $\widehat{X}$, $\widehat{\alpha}$, and $\widehat{k}_{DC}$ of the of the strongest moving target.

Input: $S(k_u, \omega)$, $\bar{x}$, k_0
Output: $\widehat{X}$, $\widehat{\alpha}$, $\widehat{k}_{DC}$, $l(\mathbf{s})$
Set: M_α, M_k, $\{\alpha_i\}_{i=1}^{M_\alpha}$, $\{k_{DC_i}\}_{i=1}^{M_k}$
Initialization: $l(1{:}3, 1{:}M_x) = 0$
for $i := 1 : M_k$ **do**
  $k_{DC}(i) := k_{DC_i}$; $\mu(i) := k_{DC}(i)/(2k_0)$
  for $j := 1 : M_\alpha$ **do**
    $\alpha(j) := \alpha_j$; $\nu(i) = \sqrt{\alpha^2(j) - \mu^2(i)}$
    $s_c := s_c[\alpha(j), k_{DC}(i), \bar{x}]$ {comp. signature (26)}
    for $n := 1 : M_x$ **do**
      $\mathbf{s} := \mathbf{s}(\alpha(j), X(n), k_{DC}(i))$ {Expressions (33) and (35)}
      $obj := l(\mathbf{s}, \mu(i), \nu(j))$ {Expression (43)}
      if $obj > l(1,n)$ **then**
        $l(1,n) := obj$, $l(2,n) := \alpha(j)$, $l(3,n) := k_{DC}(i)$
      end if
    end for
  end for
end for
$n := \text{index}\,(\max(l(1,:)))$
$\widehat{X} := X(n)$
$\widehat{\alpha} := l(2,n)\sqrt{X(n)/X_c}$
$\widehat{k}_{DC} := l(3,n)$

of a given moving target has been vertically aligned (i.e., straightened along the slow Doppler direction), the signatures of some of the remaining moving targets might be skewed because their parameters α and k_{DC} are different from those of the former moving target; therefore, off-vertical moving targets signatures with strong reflectivities might mask the vertical signatures of moving targets with weaker reflectivities. This problem can be solved by removing the strongest moving target signature from observed data once it has been detected. Algorithm 5 shows the pseudo-code for this procedure. Step 8 produces a focused image of the moving target, which has motion transformed coordinates $(\widehat{X}, \widehat{Y})$. Step 9 removes the moving target by multiplying the focused image $f(u,t)$ with a mask centered at moving target coordinates $(\widehat{X}, \widehat{Y})$.

IV. Results

The methodology developed in the previous section is now applied to synthetic and real data. The former contains point targets and an extended target, all in homogeneous background. The latter deals with real targets with simulated motion in a real background.

A. Synthetic Data

In this subsection we present results based on synthetic data aiming at the evaluation of the proposed technique. Tables I and II display the SAR mission parameters and the trajectory parameters of nine moving targets, respectively. Targets 1 to 8 are point-like, whereas target 9 is extended

Algorithm 5 Detect multiple moving targets.

Input: $S(k_u, \omega)$, $\bar{x}$, k_0
Set: $\eta := -\log(P_{F_A})$ {Set test threshold}
1: **loop**
2:   {Next moving target candidate}
3:   $(\widehat{\alpha}, \widehat{k}_{DC}, \widehat{X}) :=$ **Algorithm 4**$[s(k_u,\omega), \bar{x}, k_0]$
4:   {Estimate moving target parameters}
5:   $(\widehat{\mu}, \widehat{\nu}, \widehat{Y}, l) :=$ **Algorithm 1**$(\widehat{\alpha}, \widehat{k}_{DC}, \widehat{X})$
6:   **if** $l > \eta$ **then**
7:     {Moving target detected}
8:     $f(u,t) := \mathcal{F}^{-1}_{(k_u)}[s_c(k_u,t)]$ {Focusing moving target}
9:     $f(u,t) := f(u,t)\,\text{mask}\,(\widehat{X}, \widehat{Y})$ {Delete moving target signature}
10:     $S(k_u,\omega) := \mathcal{F}_{(u,t)}[f(u,t)]$
11:   **end if**
12: **end loop**

TABLE I
Mission parameters used in simulation.

Parameter	Value
Carrier frequency	2.5 GHz
Chirp bandwidth	50 MHz
Swath central slant-range	10 km
Platform velocity	600 km/h
Antenna azimuthal length	4 m
Antenna radiation pattern	Raised cosine
Cross-range sampling interval	1 m
Cross-range resolution	2 m
Slant-range sampling interval	1.5 m
Slant-range resolution	3 m

having 6 m in slant-range by 2 m in cross-range. The extended target was simulated with 15 point scatterers, all with the same reflectivity except for the central scatterer, which has reflectivity 10 times higher.

Fig. 5 illustrates the moving target positions at $u = 0$ and their velocities. Vertical and horizontal axes represent cross-range and slant-range recentered at the central range $\bar{x} = 10000$ m, respectively. The velocity direction of each target is represented by the respective arrow direction, while the velocity magnitude is written close to the respective arrow in km/h. The target area is rectangular centered at $(X,Y) = (\bar{x}, 0)$ and with cross-range and slant-range lengths of 512 m and 384 m, respectively. Cross-range gating can be obtained by digital spotlighting [5]. The shadowed area represents the antenna footprint at $u = 0$, whose synthetic array length is 256 m, for the parameters given in Table I.

The antenna radiation pattern is $A_0(k_u) = 1 + \cos(2\pi k_u)$ for $|k_u| \leq \pi/2$ and $A_0(k_u) = 0$ for $|k_u| > \pi/2$. Since the cross-range sampling interval is 1 m, the sampling frequency is $k_s = 2\pi$ and thus $k_s = 2\pi$, i.e., the bandwidth of a static target is half the sampling frequency k_s.

Fig. 6 displays the target area image focused for targets with relative speed $\alpha = 1.0$ and Doppler centroid $k_{DC} = 0$. The signal to clutter ratio (SCR) and the clutter to noise ratio (CNR) are both 20 dB. Targets 1, 2, and 9 are fo-

TABLE II
MOVING TARGET PARAMETERS. TARGETS 1 TO 8 ARE POINT-LIKE WHEREAS TARGET 9 IS EXTENDED [6 M (RANGE)× 2 M (CROSS-RANGE)]. COORDINATES ARE IN METERS.

	Initial coord.		Velocity		MT coord.	
Target	x_0	y_0	μ	ν	X	Y
1	-95	-80	0.00	1.0	-95.0	-80.0
2	-35	-80	0.01	1.0	-34.7	19.6
3	25	-80	0.01	0.9	25.2	31.4
4	85	-80	0.01	0.8	85.2	46.1
5	-85	80	0.00	1.2	-85.0	80
6	-25	80	0.06	1.0	-47.7	677.3
7	35	80	0.11	1.1	-22.8	1078.0
8	95	80	0.15	1.2	7.1	1331.5
9	0	0	0.01	1.0	-0.5	100

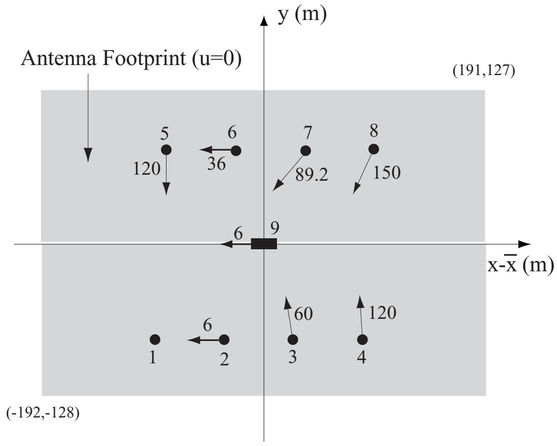

Fig. 5. Illustration of the moving target positions at $u = 0$ and their velocities. Vertical and horizontal axes represent cross-range and slant-range recentered at the central range $\bar{x} = 10000$ m, respectively. The velocity direction of each target is represented by the respective arrow direction, while the velocity magnitude is written close to the respective arrow in km/h.

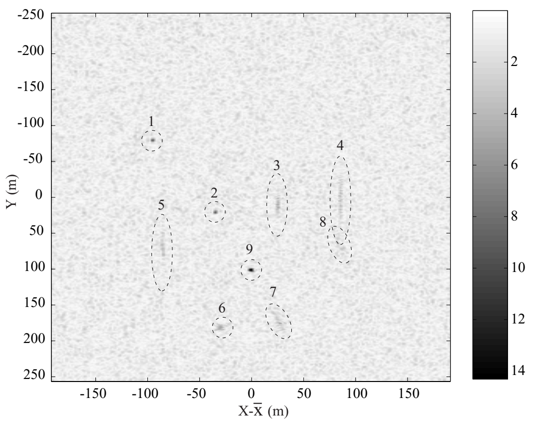

Fig. 6. Imaging of the target area focused with relative speed $\alpha = 1.0$ and Doppler centroid $k_{DC} = 0$. The signal to clutter ratio (SCR) and the clutter to noise ratio (CNR) are both 20 dB. Targets 1, 2, and 9 are focused. All other targets are defocused as their relative speeds or Doppler centroids are different from that used by the imaging algorithm. For displaying purposes, the cross-range motion transformed coordinates of targets 6 , 7, and 8 have been wrapped into the interval $[-256, 256]$ m.

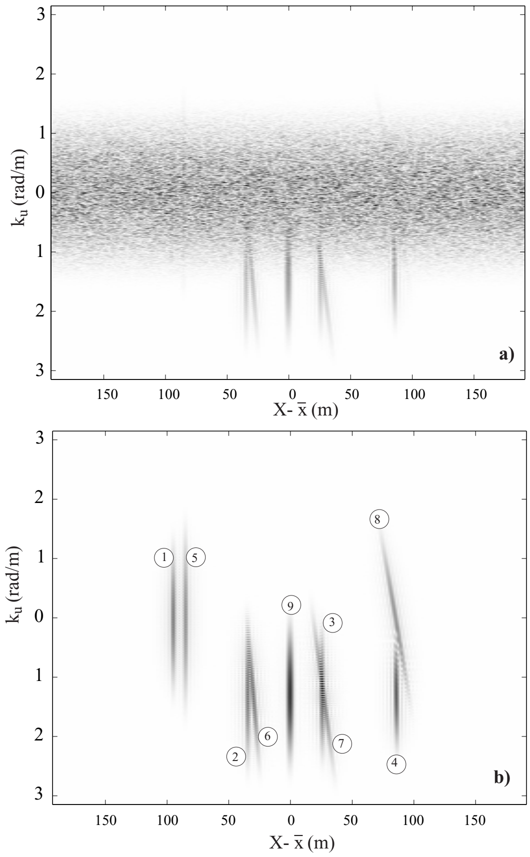

Fig. 7. Compressed signal in the (k_u, X) domain given by (26), corresponding the target area shown in Fig. (6) and using the moving target parameters $\alpha' = 1.0$, $X' = \bar{x}$, and $K'_{DC} = 0$. The signal to clutter ratio and the clutter to noise ratio are SCR = 20 dB and CNR = 20 dB, respectively, as in Fig. 6. Part a) displays moving target signatures plus clutter noise plus system noise; part a) displays only the moving target signatures.

cused. All other targets are defocused as their relative speeds or Doppler centroids are different from those used by the imaging algorithm. The cross-range coordinate at which the defocused targets are displayed exhibits errors with respect to those shown in Table II. These errors increase with the error in the Doppler centroid. For displaying purposes, the cross-range motion transformed coordinates of targets 6 , 7, and 8 have been wrapped into the interval $[-256, 256]$ m.

Fig. 7a displays the compressed signal in the $(k_u, t = 2X/c)$ domain given by (26), corresponding to the target area shown in Fig. 6 and using the moving target parameters $\alpha' = 1.0$, $X' = \bar{x}$, and $K'_{DC} = 0$. SCR and CNR are both 20 dB, as in Fig. 6. For better perception, Fig. 7b shows the moving target signatures without ground clutter and system noise. For displaying purposes, the slow-time Doppler frequency coordinates of targets 6, 7, and 8 have been wrapped into the interval $[-\pi, \pi]$ rad/m.

We see from Fig. 7 that, at least visually, only targets 6, 7, and 8 produce off-vertical aligned signatures. This was to be expected as $\tau(k_u)$ given by (28) is proportional to k_u^2 and targets 6, 7, and 8 have the larger Doppler centroids among all targets.

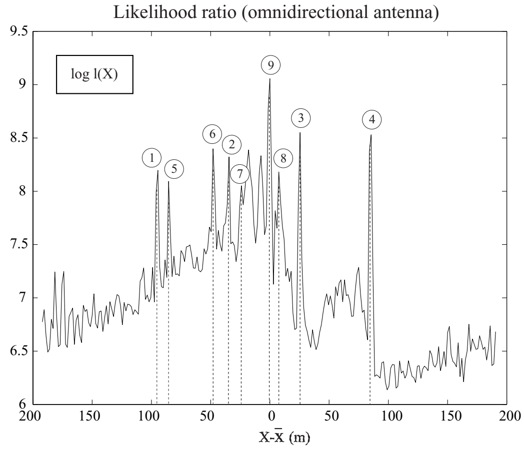

Fig. 8. Likelihood ratio test computed by Algorithm 4. For illustration purposes we have assumed an omnidirectional antenna. All moving targets originated spikes at correct moving target slant-range coordinates. The presence of two spurious spikes at slant-ranges -17 and -6 will not produces false alarms because Algorithm 5 selects only the moving target with the highest likelihood ratio in each iteration.

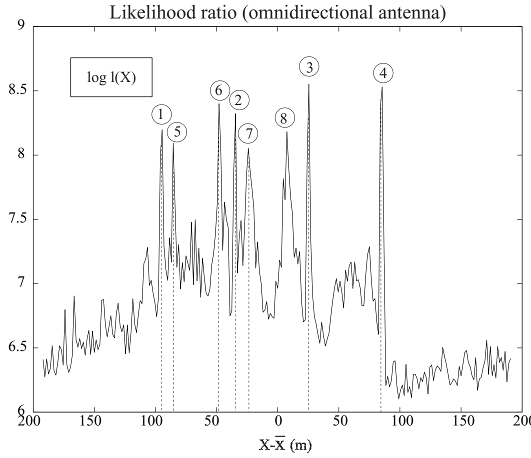

Fig. 9. Likelihood ratio test computed by Algorithm 4, using an omnidirectional antenna, after deleting the signature of target 9 (step 8 of Algorithm 5). All the remaining targets 1 to 8 originated spikes at correct moving target slant-range coordinates. The spurious spikes present in Fig. 8 at slant-ranges -17 and -6 have been removed.

TABLE III

ESTIMATION RESULTS FOR SCR $= 20\,dB$ AND CNR $= 20\,dB$. COORDINATES ARE IN METERS.

	Initial coord.		Velocity ($\times 10^3$)		GLR
Target	$\widehat{x}_0 - x_0$	$\widehat{y}_0 - y_0$	$\widehat{\mu} - \mu$	$\widehat{\nu} - \nu$	$\log l$
1	0.5	-1.8	0.12	7.9	4.17
2	0.2	0.4	0.03	3.2	8.71
3	0.2	0.5	-0.06	3.8	8.70
4	0.3	-1.0	0.03	2.4	8.62
5	-0.5	0.4	0.03	3.2	5.08
6	-0.5	1.0	-0.09	4.1	8.68
7	-1.6	0.1	-0.02	3.5	8.70
8	0.1	-1.1	0.1	3.4	5.07
9	0.5	4.0	-0.4	4.6	9.04

Fig. 8 shows the likelihood ratio test computed by Algorithm 4. For illustration purposes, an omnidirectional antenna was assumed. In fact, if the true antenna has been used $A_0(k_u, \omega)$, then the stronger signatures would have totally masked the weaker ones. The algorithm was parameterized with $M_\alpha = 30$, $\alpha_1 = 0.7$, $\alpha_{M_\alpha} = 1.3$, $M_k = 24$, $k_{DC_1} = -3$, and $k_{DC_{M_k}} = 3$, leading to sampling intervals of the relative velocity and of the Doppler centroid of 0.02 and 0.25, respectively. All moving targets originated spikes at correct moving target slant-range coordinates. Notice, however, the presence of two spurious spikes at slant-ranges -17 and -6. These spikes do not produce false alarms because Algorithm 5 selects only the moving target with the highest likelihood ratio in each iteration. It is worth noting that targets 1, 5, and 8, although not discernable among the ground clutter in Fig. 7, yield a large likelihood ratio, as we can read from Fig. 8.

Fig. 9 shows the likelihood ratio test computed by Algorithm 4 after deleting the signature of target 9 (step 8 of Algorithm 5). All the remaining targets 1 to 8 produced spikes at correct moving target slant-range coordinates. The spurious spikes present in Fig.8 at slant-ranges -17 and -6 have been removed.

Table III presents the estimation errors of parameters (x_0, y_0, μ, ν) for the nine moving targets present in the target area. Parameters t_{max}, M_μ, and M_ν of Algorithms 1, 2, and 3 were set to 2, 10, and 10, respectively. Algorithms 2 and 3 were applied in multigrid fashion using three depth levels. The last column of Table III shows, for each target, the logarithm of the likelihood ratio $\log l$. The higher values of $\log l$ correspond to targets with the higher SCNR_{opt}, or, equivalently, to targets with small spectral overlapping with the background spectrum. Using the Neyman-Pearson threshold $\eta = -\log P_F$ derived in the previous section, the upper bound for the probability of false alarm P_F allowing the detection of all moving targets is $P_F = 1.5 \times 10^{-2}$.

Roughly, the errors in x_0 and in y_0 are of the order of 0.5 m and 1 m, respectively, being lower than the slant-range and cross-range resolutions. The errors in μ and ν are of the order of 10^{-4} and 4×10^{-3}, respectively. The proposed approach yields good results even for targets with spectrum totally or almost totally superimposed on the background noise, which is the case for targets 1, 5, and 8. Extended target 9 exhibits the largest initial cross-range error. This is due to model mismatch, as we assume the targets to be point-like. Nevertheless, the estimated moving target parameters are still good for many purposes.

Table IV present results similar to Table II for SCR $=$ 14 dB and CNR $=$ 20 dB. The estimates are similar to those presented in Table III with a little degradation mainly for targets 1 and 9. The logarithm of the likelihood ratio $\log l$, compared with the previous example, decreases by, roughly, 0.5.

Table V shows the sample root mean square error (rmse) of the moving target velocity estimates $(\widehat{x}_0, \widehat{y}_0, \widehat{\mu}, \widehat{\nu})$ as a function of the slant-range velocity μ, for $\nu = 1.2$, SCR $=$ 10 dB, and CNR $=$ 20 dB. Values shown were obtained from 64 Monte Carlo simulations per point. Parameter μ determines the percentage of superposition between back-

TABLE IV
ESTIMATION RESULTS FOR $SCR = 14\,dB$ AND $CNR = 20\,dB$. COORDINATES ARE IN METERS.

	Initial coord.		Velocity ($\times 10^3$)		GLR
Target	$\widehat{x}_0 - x_0$	$\widehat{y}_0 - y_0$	$\widehat{\mu} - \mu$	$\widehat{\nu} - \nu$	$\log l$
1	0.4	-1.7	0.08	10.0	3.50
2	0.2	-0.7	0.05	3.2	8.02
3	0.2	0.5	-0.06	3.8	8.00
4	0.3	-2.8	0.14	4.4	7.94
5	-0.5	0.1	0.06	3.2	4.41
6	-0.5	1.0	-0.09	4.1	8.01
7	-3.0	1.9	-0.2	3.0	8.01
8	-0.1	-4.8	0.6	3.4	4.48
9	0.5	5.1	-0.5	4.6	8.35

TABLE V
SAMPLE ROOT MEAN SQUARE ERROR OF $(\widehat{x}_0, \widehat{y}_0, \widehat{\mu}, \widehat{\nu},)$ AS FUNCTION OF μ, FOR $\nu = 1.2$, SCR$=$ $10\,dB$, AND CNR$=$ $20\,dB$.

μ	rmse($\widehat{x}_0$)	rmse($\widehat{y}_0$)	rmse($\widehat{\mu}$)	rmse($\widehat{\nu}$)
0.005	0.64	5.6	6.9×10^{-4}	9.4×10^{-3}
0.01	0.66	3.1	3.6×10^{-4}	4.4×10^{-3}
0.015	0.22	1.9	2.1×10^{-4}	3.7×10^{-3}
0.02	0.38	2.0	2.2×10^{-4}	3.2×10^{-3}
0.025	0.33	1.3	1.6×10^{-4}	2.9×10^{-3}

ground and moving target spectra. The selected values of $\mu = 0.005, 0.01, 0.015, 0.02, 0.05$ corresponds to spectral superpositions of $84\%, 68\%, 51\%, 36\%, 20\%$, respectively. As expected, estimates improve when the spectral superposition becomes lower. For SCR$=$ $0\,dB$ and CNR$=$ $20\,dB$ the root mean square error of $\widehat{x}_0$ is very close to the values shown in Table V, whereas the root mean square error of $\widehat{y}_0$, $\widehat{\mu}$, and $\widehat{\nu}$ is higher by a factor ranging between 2 and 3.

Often, in real applications, the antenna radiation pattern, the clutter power, and the noise power are not known exactly. To illustrate the robustness of the proposed scheme to model mismatches, we have applied the proposed estimation scheme to simulated data generated with the mission parameters shown in Table I and SCR$=$ 20 dB and CNR$=$ 20 dB, but using, in the estimation algorithm and compared with the true values, an antenna radiation pattern 10% broader, a backscattering coefficient 10% higher, and a noise spectral power 10% lower. Table VI displays the moving target estimates obtained. In spite of model mismatches considered, the results exhibit only a little degradation, when compared with those of Table III computed in a model matched scenario.

TABLE VI
ESTIMATION RESULTS WITH MODEL MISMATCH. DATA WAS GENERATED WITH A RAISED COSINE SHAPED ANTENNA AND WITH SCR$= 20\,dB$ AND CNR$= 20\,dB$. THE ESTIMATION ALGORITHM ASSUMED, COMPARED WITH THE TRUE VALUES, AN ANTENNA RADIATION PATTERN 10% BROADER, A BACKSCATTERING COEFFICIENT 10% HIGHER, AND A NOISE SPECTRAL POWER 10% LOWER. COORDINATES ARE IN METERS.

	Initial coord.		Velocity	
Target	$\widehat{x}_0 - x_0$	$\widehat{y}_0 - y_0$	$(\widehat{\mu} - \mu)10^3$	$(\widehat{\nu} - \nu)10^3$
1	0.5	-1.0	0.05	3.8
2	0.2	-2.5	0.22	2.8
3	0.2	-2.2	0.18	3.8
4	0.3	-2.1	0.11	2.4
5	-0.5	-0.7	-0.16	3.2
6	-0.1	-1.6	0.17	2.4
7	-2.6	-1.2	0.15	2.5
8	-0.1	1.0	-0.21	-2.5
9	0.5	1.9	-0.20	4.6

TABLE VII
MSTAR MISSION PARAMETERS.

Parameter	Value
Carrier frequency	9.6 GHz
Chirp bandwidth	591 MHz
Swath central range	4.5 km
Depression angle	15°
Platform velocity	220 km/h
Cross-range sampling interval	0.203 m
Cross-range resolution	0.304 m
Slant-range sampling interval	0.202 m
Slant-range resolution	0.305 m

B. Real Data

In this section, images from MSTAR data public collection (see [26]) collected by Sandia National Laboratory using STARLOS sensor were used. Main mission parameters are given in Table VII. Fig. 10 shows a visible (top) and two X-Band (middle and bottom) images of the BTR 60 transport vehicle. The aspect angles of the middle and of the bottom images are nearly 0° and 90°, respectively. Fig. 11a shows an X-Band SAR image of ground plus six moving targets (transport vehicles BTR 60) focused with the *wavefront reconstruction algorithm* [10] (see Appendix C) parameterized for static target (i.e., $\mu = 0$ and $\alpha = 1$). The true vehicle positions, at $u = 0$, are indicated with numbered white circles. For better perception, Fig. 11b shows (as a negative) only the image of moving vehicles. Notice that only vehicle 1 is correctly focused and located. The remaining vehicles are blurred or wrongly located or both, as the image was focused using static target parameters, i.e., $\mu = 0$ and $\nu = 1$. The shape of the blurring depends on the moving target velocity mismatch. Target 2 is blurred along cross-range, due to a relative velocity mismatch; targets 3 and 4 are split due to a fractional Doppler centroid mismatch; finally, targets 5 and 6 are blurred in both directions, due to relative velocity and Doppler centroid mismatches.

The clutter signature in the (k_u, ω) domain was computed by reversing the wavefront reconstruction steps described in Appendix C. First, we compute expression $S(k_X, k_Y)$ [see (78)] and then interpolate this function to obtain $S_0(k_u, \omega)$ in a rectangular grid according to (75) and (76) for $\alpha = 1$. The nth moving targets signature was generated, according to (8), by computing

$$S_n(k_u, \omega) = \sum_i A_n(k_u) P_n(\omega) f_{in} e^{-j\sqrt{4k^2 - \left(\frac{k_u}{\alpha_n}\right)^2} X_{ik} + \left(\frac{k_u}{\alpha_n}\right) Y_{ik}}, \tag{48}$$

where indexes i and n denote the ith pixel of the nth moving target.

Fig. 10. Visible (top) and X-Band (middle and bottom) images of the BTR 60 transport vehicle (data from the MSTAR data public collection). Aspect angles of the middle and bottom images are nearly 0° and 90°, respectively.

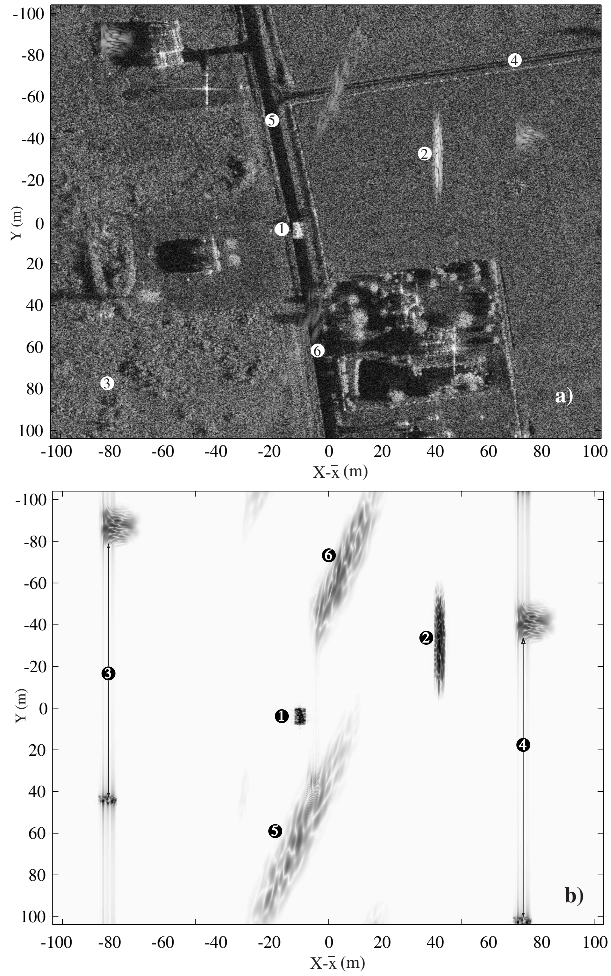

Fig. 11. Real scene focused using parameters ($\mu = 0, \nu = 1$). Part a) shows an X-Band image containing moving targets (transport vehicles BTR 60) over ground clutter. The true vehicle positions, at $u = 0$, are indicated with numbered white circles. Part b) is the same as part a), but displays only the moving targets in negative and focused with static targets parameters (i.e., $\mu = 0$ and $\nu = 1$). Both data (moving targets and ground clutter) were built using data from the MSTAR data public collection.

In a real scenario, the antenna radiation pattern can be measured or estimated from a point target. In the present data set, although there are strong targets, we are not sure if they are point-like. For this reason we resort to power spectrum estimation tools to determine the shape of the antenna radiation pattern $|A_0(k_u,\omega)|$, the variance $\beta|A_0(k_u)|^2+\gamma$ of the clutter plus noise signature $w(k_u,t)$, and the pulse $P(\omega)$. Concerning the variance $\beta|A_0(k_u)|^2+\gamma$, an homogeneous rectangular region (north-east and south-west coordinates $(100,-60)$ and $(5,20)$, respectively, in Fig. 11) was selected, then computed the sample mean of $|w(k_u,t)|^2$ along t coordinates and finally applied smoothing along k_u coordinate. The magnitude of pulse function $|P(\omega)|$ was determined using a similar procedure.

Fig. 12 shows the estimated magnitude of the antenna radiation pattern. Notice that the cross-range sampling frequency k_s is only marginally above the Nyquist frequency, thus placing stringent performance requirements on the moving target detector, as these target signatures will always overlap, at least partially, the clutter signature, regardless of the slant-range velocity.

In simulating the moving targets signatures, $A_0(k_u)$ has been used as antenna radiation pattern and the respective estimated magnitudes as the pulse function $P(\omega)$. One notes that, although $|A_0(k_u)|$ and $|P(\omega)|$ might be different from $A_0(k_u)$ and $P(\omega)$, this has no impact on the results, as the performance of the detection and estimation schemes proposed in the previous section depends only on the magnitudes of those functions.

Table VIII shows the parameters of the six vehicles moving in the target area. The SCR with respect to the strongest moving scatterer is 30dB for target 1 and 20dB for targets 2 to 6. Initial positions x_0 and y_0 are relative to the strongest moving scatter. The Doppler centroids nor-

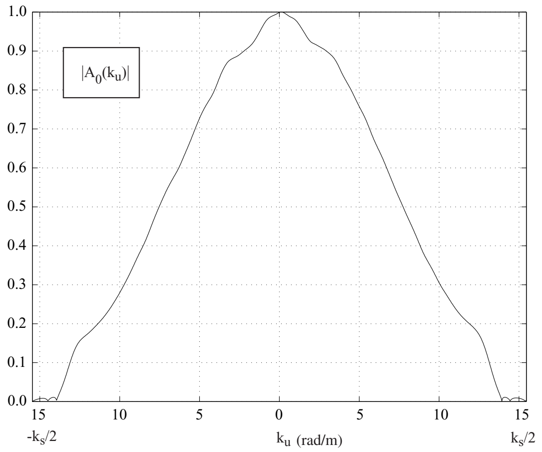

Fig. 12. Estimated magnitude of the antenna pattern $A_0(k_u)$.

TABLE VIII
MOVING TARGET PARAMETERS OF THE SIX TANKS SPOTTED IN FIG. 11. COORDINATES ARE IN METERS.

	Initial coord.		Rel. vel.		Vel. (km/h)
Target	x_0	y_0	μ	ν	$\lvert v\rvert$
1	-12.5	0	0.0	1.0	0
2	40	-40	0.0	1.1	22
3	-80	80	0.0385	1.0	8.5
4	70	-76	0.0385	1.0	8.5
5	-21	-52	0.1346	0.8	53
6	-4	65	-0.1346	1.2	53

malized to the Nyquist frequency of targets 1-2, 3-4, 5 and 6 are 0.0, 0.5, 1.75 and -1.75, respectively.

Table IX presents the estimation errors. Excepting the initial cross-range position y_0 of targets 5 and 6, all estimates are very accurate. The error of the initial position x_0 and of the motion transformed coordinates X and Y are less than 1 m; the error of the slant-range velocity μ and of the cross-range velocity estimates are less 0.4% and 1%, respectively. Concerning the initial cross-range position y_0, targets 5 and 6 present the larger errors, the reason being the extended nature of the targets. In fact, a thorough inspection of the vertical tank shown in Fig. 10 reveals that the most predominant scatterers are very close in reflectivity and aligned along the cross-range coordinate. Theses two targets interfere generating an equivalent Doppler domain dependent reflectivity $f(k_u)$ that distorts the antenna radiation pattern $A(k_u)$, leading to errors on the relative slant-range velocity. This phenomenon is equivalent to

TABLE IX
ESTIMATION RESULTS FOR THE SIX EXTENDED TARGETS SHOWN IN FIG. 11. COORDINATES ARE IN METERS.

	Initial coord.		MT coord.		Rel. vel. ($\times 10^2$)	
Tar.	$\widehat{x}_0 - x_0$	$\widehat{y}_0 - y_0$	$\widehat{X} - X$	$\widehat{Y} - Y$	$\widehat{\mu} - \mu$	$\widehat{\nu} - \nu$
1	0.00	-2.2	0.0	0.0	0.05	0.01
2	-0.18	-0.86	-0.18	0.0	0.02	0.02
3	0.00	-2.03	-0.08	-0.02	0.04	-0.004
4	0.01	-1.3	0.09	0.2	0.03	-0.073
5	-0.11	5.01	-0.01	-1.15	-0.15	0.021
6	-0.36	-8.36	0.12	1.00	-0.20	-1.00

having targets with reflectivities dependent on the aspect angle. Surprisingly, the errors induced by these model mismatches are perfectly acceptable with respect to the slant-range velocity itself, the same not being true for the initial position y_0. While we obtained errors smaller than 2 m for those targets exhibiting a clearly predominant scatterer, this was not the case with targets 5 and 6, for which we obtained errors of the initial cross-range positions of 5.01 m and −8.36 m, respectively. Recall that $\widehat{y}_0 = (\widehat{\mu}\widehat{X} + \widehat{\nu}\widehat{Y})/\widehat{\alpha}$ and that $\widehat{X} \simeq 4500$ m; therefore, to have errors less than, say, 1 m in $\widehat{y}_0$, the relative slant-range estimate $\widehat{\mu}$ must exhibit an absolute error smaller than 2.2×10^{-4}. This is not achieved for targets 5 and 6, where the errors of the relative slant-range velocities are -1.5×10^{-3} and -2.2×10^{-3}, respectively.

C. Limitations of the Proposed Method

The proposed method was developed under two main assumptions: 1) targets are point-like and 2) the slant-range velocity satisfies $\mu \ll c/(BD_y)$. The first assumption is violated when the target is extended and does not have any predominant scatterer; the second assumption is more restrictive in SAR systems with high resolution in the slant-range direction (large pulse bandwidth B) and low resolution in the cross-range direction (large cross-range length D_y), not a very common scenario.

Concerning limitation 1), the mean $E[s_i] = f a_i$ of random variable s_i, introduced in (35), is not valid in the case of an extended target. A solution to this problem is modelling extended targets as arrays of discrete point targets, each one with reflectivity f_i and distance d_i to a reference point. The mean value of s_i would then be given by $E[s_i] = a_i \sum_n f_n e^{-j\frac{k_{u_i} d_n}{\alpha}}$. The determination of f_i and d_i, for $i = 1, \ldots$ is out of the scope of this paper. Anyway, as most natural and man-made extended targets have predominant scatterers exhibiting nearly point-like behavior, the proposed approach applies largely to these targets.

Concerning limitation 2), it can be overcome by partitioning the fast-time frequency interval into N subsets of equal length such that the condition $\mu \ll (cN)/(BD_y)$ becomes true, and apply the proposed method to one of the resulting data sets. If the accuracy of the estimates is poor, one may compute the sample mean of the moving target parameter estimates from all the data sets.

V. CONCLUSIONS

The paper presents a novel methodology to detect multiple moving targets in stripmap SAR and to estimate their trajectory parameters using a single sensor. By taking into account the antenna radiation pattern, the proposed algorithm determines, for each moving target (assumed to have constant velocity), not only the target location in the slant-plane, but also the two components of the velocity vector (cross-range and slant range velocities). Therefore, *the so-called azimuth position uncertainty* inherent to single sensor based systems is solved.

Whatever the domain (i.e., space, frequency, or mixed) adopted to detect the moving targets and estimate their parameters, their signatures are spread over a two-dimensional set, thus introducing complexity in any processing scheme. To reduce this complexity, a step was introduced that compresses moving target signatures along the slow-time Doppler domain for a given fast-time. Besides compressing moving targets signatures, this step yields, for each moving target candidate, the slant-range motion transformed estimate and an approximate estimate of the relative speed.

A generalized likelihood ratio test approach was then adopted to detect moving targets and derive their trajectory parameters. Determining the maximum likelihood estimate necessary to compute the generalized likelihood ratio test would amount to a multidimensional nonlinear optimization of the unknown parameters, with unbearable computational burden. Instead of computing the exact maximum likelihood estimate, a suboptimal approach was adopted that iteratively maximizes the likelihood function on given subsets of the search space. The detection threshold was set according to the Neyman-Pearson criterion. Is was found that in the ideal case of perfect knowledge of density parameters (clairvoyant detector), the detector performance depends only on optimal signal to clutter plus noise ratio (SCNR_{opt}) obtained with the matched filter (filter matched to the signal signature immersed in clutter plus system noise). As an indication of the detector performance, for a false probability of 10^{-2} we have a detection probability greater that 0.8 for $\mathrm{SCNR}_{opt} \gtrsim 10$.

The effectiveness of the proposed method was illustrated with synthetic and real data. In the former case we simulated an S-band image with 8 point moving targets and an extended target with a predominant scatterer. For $\mathrm{SCR} = 20\,\mathrm{dB}$ and $\mathrm{CNR} = 20\,\mathrm{dB}$ we obtained estimates of the relative slant-range and cross-range velocities within an error of, approximately, 0.01% and of 0.4%, respectively. The initial position coordinates displayed errors less than the slant-range and cross-range resolutions. These values only degrade slightly for $\mathrm{SCR} = 14\,\mathrm{dB}$ and $\mathrm{CNR} = 20\,\mathrm{dB}$.

Real data results were obtained from X-Band images of the MSTAR public data collection collected by Sandia National Laboratory using STARLOS sensor. The ground clutter and moving target signatures (transport vehicles BTR 60) were obtained by resynthesizing the respective reflectivities using an inverse wavefront reconstruction algorithm. The SCR of all moving targets, measured with respect to the strongest moving scatter was less than 20dB. With the exception of the initial cross-range position, all estimates were very accurate. The errors of the initial position x_0 and of the motion transformed coordinates X and Y are less than 1 m; the error of the slant-range velocity μ and of the cross-range velocity estimates are less 0.4% and 1%, respectively. Concerning the initial cross-range positions, we obtained errors smaller than 2 m for those targets exhibiting a clearly predominant scatterer. This is was not the case for targets 5 and 6 that had two predominant targets with similar reflectivity at the same cross-range motion transformed coordinate. For this targets the error of the initial cross-range position is 5.01 m for target 5 and -8.36, for target 6.

The major limitations of the proposed method are the assumptions of 1) independence of the antenna radiation pattern with respect to the fast-time frequency and 2) of point-like moving targets. The first limitation can be circumvented by partitioning the fast-time frequency into small subsets and applying the proposed technique to the resulting data bases. The solution for the second limitation is modelling extended targets as arrays of discrete point targets, each one with a given reflectivity and distance to a reference point. This approach is to be exploited in future work. Anyway, as most natural and man-made extended targets have predominant scatterers exhibiting nearly point-like behavior, the proposed approach applies generally to these targets.

Appendices

A. Fast-time Compressed Signal

We wish to compute the fast-time compressed signal

$$s_{mc}(k_u,t) \equiv \mathcal{F}^{-1}_{(\omega)}\left[S_m(k_u,\omega)P^*(\omega)e^{j\psi'(k_u,\omega)}\right], \tag{49}$$

where $S_m(k_u,\omega)$ is given by (24) and $\psi'(k_u,\omega)$ is given by (12) for moving target parameters $(\alpha', X', 0)$. Introducing $S_m(k_u,\omega)$ and $\psi'(k_u,\omega)$ into (49), we obtain

$$s_{mc}(k_u,t) = \mathcal{F}^{-1}_{(\omega)}\left[|P(\omega)|^2 A(k_u) f e^{-j\xi(k_u,\omega)} e^{-jk_u(Y/\alpha)}\right] \tag{50}$$

with

$$\xi(k_u,\omega) = 2k\left[\sqrt{1-\left(\frac{k_u}{2k\alpha}\right)^2}X - \sqrt{1-\left(\frac{k_u}{2k\alpha'}\right)^2}X'\right]. \tag{51}$$

Expanding ξ in Taylor series about $k_u = 0$, we get

$$\xi(k_u,\omega) = 2k\left[(X-X') - \frac{1}{2}\left(\frac{k_u}{2k}\right)^2\left(\frac{X}{\alpha^2} - \frac{X'}{\alpha'^2}\right)\right] + \Delta, \tag{52}$$

where $|\Delta| \lessapprox \frac{k_u^4}{64k^3}\left|\frac{X}{\alpha^4} - \frac{X'}{\alpha'^4}\right|$. Assuming that $\left|\frac{X}{\alpha^4} - \frac{X'}{\alpha'^4}\right| \ll \frac{64\pi k^3}{|k_u|^4_{max}}$, then, phase Δ in (52) satisfies $|\Delta| \ll \pi$, thus being negligible.

By the same token we have

$$\frac{k_u^2}{4k}\left(\frac{X}{\alpha^2} - \frac{X'}{\alpha'^2}\right) \simeq \frac{k_u^2}{2k_0}\left(\frac{X}{\alpha^2} - \frac{X'}{\alpha'^2}\right)(1 - \frac{k}{2k_0}), \tag{53}$$

for $\left|\frac{X}{\alpha^4} - \frac{X'}{\alpha'^4}\right| \ll \frac{4\pi k_0^3}{|k_u|^2_{max}(\Delta k)^2}$, with $\Delta k = k - k_0$.

Noting that $k = k_0 + \omega/c$, inserting (53) into (52) and the resulting expression for $\xi(k_u,\omega)$ into (50), we obtain

$$s_{mc}(k_u,t) = \mathcal{F}^{-1}_{(\omega)}\left[|P(\omega)|^2 A(k_u) f e^{-j\omega\tau(k_u)} e^{-j\eta(k_u))}\right] \tag{54}$$

where

$$\tau(k_u) \equiv \frac{2(X-X')}{c} + \frac{1}{c}\left(\frac{k_u}{2k_0}\right)^2\left(\frac{X}{\alpha^2} - \frac{X'}{\alpha'^2}\right) \tag{55}$$

$$\eta_n(k_u) \equiv -\frac{k_u^2}{4k_0}\left(\frac{X}{\alpha^2} - \frac{X'}{\alpha'^2}\right) + k_u\frac{Y}{\alpha} + \varphi, \tag{56}$$

with $\varphi = 2k_0(X - X')$.

Assume that the variations of $A(k_u, \omega)$ are neglegible within the frequency support of $P(\omega)$. According to (21), this is true if $2\mu\Delta k \ll \Delta k_u$, where $\Delta k_u \simeq (4\pi/Dy)$ and $\Delta k = 2\pi B/c$ (B is the pulse bandwidth) are the bandwidths of $A_0(k_u)$ and $P(kc)$, respectively. The inequality above can then be the rewritten as $\mu \ll c/(BD_y)$.

Under these conditions the inverse Fourier transform (54) yields

$$s_{mc}(k_u, t) = fR_p[t - \tau(k_u)]A(k_u)e^{-j\eta(k_u)}. \tag{57}$$

where $R_p(t)$ is the auto-correlation of the transmitted pulse $p(t)$.

B. Background statistics

According to (26) and(30), the static ground term w is

$$w(k_u, t) = \mathcal{F}^{-1}_{(\omega)}\left[S_0(k_u, \omega)P^*(\omega)e^{\psi'(k_u,\omega)}\right], \tag{58}$$

where phase $\psi'(k_u, \omega)$ is given by (12). Introducing $S_0(k_u, \omega)$ [see (25)] into (58) yields

$$\begin{aligned} &w(k_u, t) = \\ &\mathcal{F}^{-1}_{(\omega)}\left[|P(\omega)|^2 A_0(k_u)\sum_n f_n e^{-j\xi_n(k_u,\omega)}e^{-jk_uY_n}\right] \end{aligned} \tag{59}$$

with

$$\xi_n(k_u, \omega) = 2k\left[\sqrt{1 - \left(\frac{k_u}{2k}\right)^2}X_n - \sqrt{1 - \left(\frac{k_u}{2\alpha' k}\right)^2}X'\right]. \tag{60}$$

Proceeding as in Appendix A, we conclude that

$$w(k_u, t) = A_0(k_u)\sum_n f_n R_p[t - t_n(k_u)]e^{-j\eta_n(k_u)},$$

where

$$\begin{aligned} t_n(k_u) &\equiv \frac{2(X_n - X')}{c} + \frac{1}{c}\left(\frac{k_u}{2k_0}\right)^2\left(X_n - \frac{X'}{\alpha'^2}\right) && (61)\\ \eta_n(k_u) &\equiv -\frac{k_u^2}{4k_0}\left(X_n - \frac{X'}{\alpha'^2}\right) + k_uY_n + \varphi. && (62) \end{aligned}$$

Let us assume that the number of scatterers per resolution cell is large, none is predominant, the echo amplitudes f_n, $n = 0, 1, \cdots, N-1$ are mutually independent and have phase uniformly distributed in a 2π interval independent of its amplitude. Under these conditions $w(k_u, t)$ has complex Gaussian density [27], and the random complex amplitude f_n has mean value and variance

$$\begin{aligned} E[f_n] &= E[|\rho_n|]\underbrace{E[e^{j\phi}]}_{=0} = 0 && (63)\\ E[f_n f_m^*] &= \delta_{mn}\sigma_n^\circ, && (64) \end{aligned}$$

where δ_{mn} is the Kronecker symbol, and σ_n° is the nth scatterer radar cross-section. This statistics implies that $E[w(k_u, t)] = 0$ and that the covariance $C_w(k_{u_1}, k_{u_2}) \equiv E[w(k_{u_1}, t)w^*(k_{u_2}, t)]$ be given by

$$\begin{aligned} &C_w(k_{u_1}, k_{u_2}) = \\ &\quad A_0(k_{u_1}, k_{u_2})\sum_n P\sigma_n^\circ R_n e^{-j[\eta_n(k_{u_1}) - \eta_n(k_{u_2})]}, \end{aligned} \tag{65}$$

where

$$\begin{aligned} A_0(k_{u_1}, k_{u_2}) &\equiv A_0(k_{u_1})A_0^*(k_{u_2}) && (66)\\ R_n &\equiv R_p[t - t_n(k_{u_1}]R_p^*[t - t_n(k_{u_2})]. && (67) \end{aligned}$$

According to expression (62) it follows that

$$\begin{aligned} &\eta_n(k_{u_1}) - \eta_n(k_{u_2}) = \\ &\qquad X_n\underbrace{\frac{k_{u_2}^2 - k_{u_1}^2}{4k_0}}_{k_a} + Y_n\underbrace{(k_{u_1} - k_{u_2})}_{k_b} \\ &\qquad + \underbrace{\frac{X'}{\alpha'^2}\frac{k_{u_1}^2 - k_{u_2}^2}{4k_0}}_{\xi} && (68)\\ &\qquad = X_nk_a + Y_nk_b + \xi. && (69) \end{aligned}$$

Thus,

$$\begin{aligned} C_w(k_{u_1}, k_{u_2}) &= A_0(k_{u_1}, k_{u_2})e^{-j\xi} && (70)\\ &\times\sum_n \sigma_n^\circ R_n e^{-jk_aX_n}e^{-jk_bY_n}. && (71) \end{aligned}$$

Function $R_p[t - t_n(k_u)]$ has its energy highly concentrated about $t_n(k_u) = t$, or, according to (61), about

$$X_n = X'\frac{ct + 2 + \left(\frac{k_u}{2\alpha' k_0}\right)^2}{2 + \left(\frac{k_u}{2k_0}\right)^2}.$$

Assuming that $|k_u/(2\alpha' k_0)|^2 \ll 1$, then $R(X_n, k_{u_1}, k_{u_2}) \equiv R_n$ has its energy clustered about $X_n = X' + (c/2)t$.

Having in mind that the backscattering coefficient $\sigma^\circ(X, Y)$ at (X, Y) is given by

$$\sigma^\circ(X, Y) \equiv \Delta^{-1}\sum_{\{n:(X_n, Y_n)\in\Delta(X,Y)\}}\sigma_n^\circ,$$

where $\Delta(X, Y)$ is a small rectangle of area Δ centered at (X, Y), then expression (70) can be approximated by the integral

$$\begin{aligned} &C_w(k_{u_1}, k_{u_2}) = \\ &\quad A(k_{u_1}, k_{u_2}, \boldsymbol{\theta}_0)e^{-j\xi}\int_{-\infty}^{\infty}\int_{Y_1}^{Y_2} R(X, k_{u_1}, k_{u_2}) \\ &\quad\times\sigma^\circ(X, Y)e^{-jk_aX}e^{-jk_bY}dX\,dY \end{aligned} \tag{72}$$

The high resolution of $R(X, k_{u_1}, k_{u_2})$, with respect to X allows writing

$$\begin{aligned} &C_w(k_{u_1}, k_{u_2}) = A_0(k_{u_1}, k_{u_2})e^{-j\xi} \\ &\underbrace{\int_{-\infty}^{\infty} R(X, k_{u_1}, k_{u_2})e^{-jk_aX}\,dX}_{S(k_{u_1}, k_{u_2})}\underbrace{\int_{Y_1}^{Y_2}\sigma^\circ(X'', Y)e^{-jk_bY}dY}_{\sigma^\circ(X'', k_b)}, \end{aligned}$$

with $X'' \equiv X' + (c/2)t$.

Function $S(k_{u_1}, k_{u_2})$ is the Fourier transform of $R(X, k_{u_1}, k_{u_2})$ with respect to X computed at $k_a = (k_{u_2}^2 - k_{u_1}^2)/(4k_0)$ and $\sigma^\circ(X, k_b)$ is the Fourier transform of of $\sigma^\circ(X,Y) I_{[Y_1,Y_2]}(Y)$ with respect to Y, where $I_{[Y_1,Y_2]}(Y)$ is the indicator function of set $[Y_1, Y_2]$.

Assuming that $\sigma^\circ(X,Y)$ is constant with respect to $Y \in [Y_1, Y_2]$, i.e., $\sigma^\circ(X,Y) = \sigma^\circ(X)$ for $Y \in [Y_1, Y_2]$, then $\sigma^\circ(X'', k_b) = e^{-k_b \overline{Y}} L \sigma^\circ(X'') \,\mathrm{Sa}\,(k_b L/2)$, with $\overline{Y} = (Y_1 + Y_2)/2$, $L = Y_2 - Y_1$, and $\mathrm{Sa}\,(x) \equiv \sin(x)/x$. Moreover, if $k_b = k_{u_2} - k_{u_2} = 2l\pi/L$, with $l \in \mathcal{Z}$, then

$$C_w(k_{u_1}, k_{u_2}) = \sigma^\circ L E_{R_p} |A_0(k_u)|^2 \delta_l \qquad (73)$$

where $\sigma^\circ \equiv \sigma^\circ(X)$, $E_{R_p} \equiv S(k_u, k_u)$ denotes the energy of $|R_p[cX/2]|^2$, and δ_l denotes the unitary impulse.

If $\sigma^\circ(X,Y)$ is not constant with respect to Y, then function $\sigma^\circ(X, k_{u_1} - k_{u_2})$ becomes more broaden. However, since $|k_a| \ll 1$, it is still reasonable to assume in most situations that $S(k_{u_1}, k_{u_2})$ is much more smooth than $\sigma^\circ(X, k_{u_1} - k_{u_2})$. In this case we have

$$C_w(k_{u_1}, k_{u_2}) = e^{-j\xi} E_{R_p} A_0(k_{u_1}, k_{u_2}) \sigma^\circ(X'', k_{u_2} - k_{u_1}). \qquad (74)$$

C. Wavefront Reconstruction Algorithm

This appendix summarizes the matched filtering approach to SAR imaging.

Let k_X and k_Y be defined as

$$k_X = \sqrt{4k^2 - \left(\frac{k_u^2}{\alpha}\right)^2}, \qquad (75)$$

$$k_Y = \frac{k_u}{\alpha}, \qquad (76)$$

for $(\omega, k_u) \in S_{PA}$, where S_{PA} is the frequency support of $P(\omega)A(k_u, \omega)$. The received signal (8) can thus be written as

$$S(k_u, \omega) = P(\omega) A(k_u, \omega) f e^{-jk_X X} e^{-jk_Y Y}. \qquad (77)$$

We assume that $4k^2 - (k_u/\alpha)^2 > 0$ for $(\omega, k_u) \in S_{PA}$. This condition, always satisfied in any application of interest, implies that k_X is always real.

In the case of an extended moving target with all its elementary scatterers having the same relative speed α, the returned signal is

$$S(k_X, k_Y) = P(\omega) A(k_u, \omega) \underbrace{\int\int f(x,y) e^{-jk_X X} e^{-jk_Y Y} dx dy}_{F(k_X, k_Y)}. \qquad (78)$$

Estimating $f(X,Y)$ is therefore an inverse problem that can be addressed under the regularization [28], the Bayesian [29], or the matched filtering [7, ch. 2] frameworks. The matched filtering approach is the most frequent used in SAR applications, as it is lighter, from the computational point of view, and robust to model mismatches.

Matched filtering is performed both in fast-time and in slow-time. It amounts to compute the inverse Fourier Transform

$$\begin{aligned} \hat{f}(X, Y, \alpha) &= \mathcal{F}^{-1}_{(k_X, k_Y)} [P^*(\omega) A^*(k_u, \omega) \\ &\times \; P(\omega) A(k_u, \omega) F(k_X, k_Y)]. \end{aligned} \qquad (79)$$

In summary, the matched filtering approach to SAR imaging implements the following steps:
1. Computes the two-dimensional Fourier transform of data $s(u,t)$
2. Implements the change of variables (75) and (76)
3. Computes the two-dimensional inverse Fourier transform (79).

This imaging scheme belongs to a class of algorithms often referred to as *wavenumber domain* or $\omega - k$ processors, or *wave front reconstruction* in the Soumekh's terminology [10], [5]. The roots of this imaging scheme can be traced back to seismic signal processing for imaging the substrata of earth [30], [31]. This ideas were latter applied to imaging of SAR data (see, e.g.,[32], [33], [34]).

List of Symbols

$a(\phi, \theta, \omega)$	Two-way antenna radiation pattern at frequency $\omega + \omega_0$
$A(k_u, \omega)$	Slow-time Doppler two-way antenna radiation pattern
B	Pulse bandwidth
c	Speed of light
$C_w(k_{u_1}, k_{u_1})$	Covariance of $w(k_u, t)$ at time t
D_y	Cross-range aperture length
E_{R_p}	Energy of $R_p(t)$
E_p	Energy of $p(t)$
f	Point target refectivity
$\mathcal{F}$	Fourier transform operator
$\mathcal{F}^{-1}$	Inverse Fourier transform operator
$g(k_x, k_y)$	Fourier transform of the electric field in the antenna aperture
k	Wavenumber
k_{DC}	Doppler centroid
k_s	Nyquist cross-range frequency
k_x	Slant-range spatial frequency
k_y	Cross-range spatial frequency
k_u	Slow-time Doppler (frequency) domain (spatial frequency)
$l(s)$	Likelihood ratio
L	Cross-range length of the target area
$\mathcal{N}(\mu, \mathbf{C})$	Normal probability density function of mean vector $\boldsymbol{\mu}$ and covariance matrix $\mathbf{C}$
$p(t)$	Transmitted radar signal
$p(\mathbf{s}\|f, \boldsymbol{\theta})$	Probability density function of vector $\mathbf{s}$ parameterized with f and $\boldsymbol{\theta}$
$P(\omega)$	Fourier transform of the transmitted radar pulse
P_D	Probability of detection
P_{F_A}	Probability of false alarm
r	Radial distance
$R_p(t)$	Deterministic autocorrelation of $p(t)$
$s(u,t)$	Spatial signature of a scene
$s(u,\omega)$	Fourier transform of $s(u,t)$ w.r.t. t
$S(k_u, \omega)$	Fourier transform of $s(u,t)$ w.r.t. u and t
$\overline{S}(\Omega, \omega)$	Discrete Fourier transform of $s(n\Delta u, \omega)$

$s_c(k_u,t)$	Compressed signature in the (k_u,t) domain
t	Fast-time domain
u	Slow-time domain (position of the antenna)
v_x	Slant-range velocity of a moving target
v_y	Cross-range velocity of a moving target
v	Velocity magnitude of a moving target
x	Slant-range domain
x_0	Initial $(u=0)$ slant-range coordinate of a moving target
X	Motion transformed slant-range coordinate
$\bar{x}$	Center of the slant-range interval corresponding to the swath
y	Cross-range domain
y_0	Initial $(u=0)$ cross-range coordinate of a moving target
Y	Motion transformed cross-range coordinate
α	Relative speed of a moving target
η	Detection threshohd
θ	Aspect angle of a target
$\boldsymbol{\theta}$	Moving target parameter vector $(\mu,\nu\, X,Y)$
λ	Wavelength
μ	Relative slant-range velocity of a moving target
ν	Relative cross-range velocity of a moving target
σ^0	Backscattering coefficient
σ^n	System noise spectral power
ϕ	Longitude of a target
ω	Low-pass equivalent frequency domain
ω_0	Carrier frequency
$\psi(k_u,\omega)$	Phase of the scene signature in the Fourier domain
Δu	Cross-range spatial sampling

Acknowledgments

The authors would like to acknowledge the Air Force Research Laboratory (AFRL) and the Defense Advanced Research Projects Agency (DARPA) for MSTAR data they promptly made available to us.

References

[1] D. Munson and R. Visentin, "A signal processing view of strip-mapping synthetic aperture radar," *IEEE Transactions on Acoustics, Speech, and Signal Processing*, vol. 37, no. 12, pp. 2131–2147, 1989.

[2] R. Raney, "Synthetic aperture imaging radar and moving targets," *IEEE Transactions on Aerospace and Electronic Systems*, vol. 7, no. 3, pp. 499–505, 1971.

[3] A. Freeeman and A. Currie, "Synthetic aperture radar (SAR) images of moving targets," *GEC Journal of Research*, vol. 5, no. 2, pp. 106–115, 1987.

[4] S. Barbarossa, "Detection and imaging of moving objects with synthetic aperture radar," *IEE Proceedings-F*, vol. 139, no. 1, pp. 79–88, February 1992.

[5] M. Soumekh, "Reconnaissance with ultra wideband UHF synthetic aperture radar," *IEEE Signal Processing Magazine*, pp. 21–40, July 1995.

[6] J. Ender, "Detection and estimation of moving target signals by multi-channel SAR," in *Proceedings of the EUSAR'96*, 1996, pp. 411–417.

[7] M. Soumekh, *Synthetic Aperture Radar Signal Processing with MATLAB algorithms*, Wiley-Intercience, 1999.

[8] J. Ender, *MTI SAR Processing*, Carl-Cranz-Gesellschaft (Association for Continuing Education in Science and Technology), 1997, Course Notes SE 2.06 on SAR - Principles and Applications.

[9] S. Werness, W. Carrara, L. Joyce, and D. Franczak, "Moving target algorithm for SAR data," *IEEE Transactions on Aerospace and Electronic Systems*, vol. 26, pp. 57–67, 1990.

[10] M. Soumekh, *Fourier Array Imaging*, Prentice Hall, 1994.

[11] S. Young, N. Nasrabadi, and M. Soumekh, "SAR moving target detection and identification using stochastic gradient techniques," in *Proceedings of the International Conference on Acoustics, Speech, and Signal Processing – ICASSP'95*, 1995, pp. 2145–2148.

[12] R. Perry, R. DiPietro, and R. Fante, "SAR imaging of moving targets," *IEEE Transactions on Aerospace and Electronic Systems*, vol. 35, no. 1, pp. 188–200, 1999.

[13] M. Kirscht, "Detection, velocity estimation and imaging of moving targets with single-channel SAR," in *Proceedings of the EUSAR'98*, 1998, pp. 587–590.

[14] L. Brennan, L. Mallett, and I. Reed, "Adaptive arrays in airborne MTI," *IEEE Transactions on Aerospace and Electronic Systems*, vol. 9, no. 2, pp. 607–615, Sept. 1976.

[15] J. Ward, "Space-time adaptive processing for airborne radar," Technical report 1015, Lincoln Laboratory, MIT, Dec. 1994.

[16] R. Klemm, "Introduction to space-time adaptive processing," *IEE Electronics & Communication Engineering Journal*, vol. 911, no. 1, pp. 5–12, 1999.

[17] J. Ender, "Subspace transformation techniques applied to multichannel SAR/MTI," in *Proceedings of the 1999 International Geoscience and Remote Sensing Symposium-IGARSS'99*, 1999, pp. 38–40.

[18] B. Friedlander and B. Porat, "VSAR: A high resolution radar system for ocean imaging," *IEEE Transactions on Aerospace and Electronic Systems*, vol. 34, pp. 755–776, 1998.

[19] G. Wang and X. Xia, "Dual-speed SAR imaging of moving targets," in *Proceedings of the IEEE Radar Conference*, 1999, pp. 227–232.

[20] G. Wang, X. Xia, V. Chen, and R. Fiedler., "Detection, location and imaging of fast moving targets using multi-frequency antenna array SAR (MF-SAR)," in *Proceedings of the EUSAR'2000*, 2000, pp. 557–560.

[21] P. Marques and J. Dias, "Moving targets in synthetic aperture images: A Bayesian approach," in *IEEE International Conference on Image Processing-ICIP'00*, 2000, vol. VI, pp. 685–688.

[22] M. Born and E. Wolf, *Principles of Optics*, Pergamon Press, 6 edition, 1983.

[23] R. Collin, *Antennas and Radiowave Propagation*, McGraw Hill, 1987.

[24] S. Kay, *Fundamentals of Statistical Signal Processing. Detection Theory*, Prentice-Hall, Englewood Cliffs, NJ, 1998.

[25] S. Haykin, *Communication Systems*, John Wiley & Sons, New York, 2001.

[26] T. Ross, S. Worrell, V. Velten, J. Mossing, and M. Bryant, "Standard SAR ATR evaluation experiments using the MSTAR public release data set," in *SPIE Proceedings: Algorithms for Synthetic Aperture Radar Imagery V*, 1998, vol. 3370, pp. 566–573.

[27] C. Jakowatz, D. Wahl, P. Eichel, D. Ghiglia, and P. Thompson, *Spotlight-Mode Synthetic Aperture Radar: A Signal Processing Approach*, Kluwer Academic Publishers, Boston, 1996.

[28] F. Natterer, *The Mathematics of Computerized Tomography*, B.G. Teubner, Stuttgart, 1986.

[29] S. Geman and D. Geman, "Stochastic relaxation, Gibbs distribution and the Bayesian restoration of images," *IEEE Transactions on Pattern Analysis and Machine Intelligence*, vol. PAMI-6, no. 6, pp. 721–741, November 1984.

[30] H. Stolt, "Migration by Fourier transform," *Geophysics*, vol. 1, pp. 23–48, February 1978.

[31] J. Gazdag and P. Sguazzero, "Migration of seismic data," *Proceedings of the IEEE*, vol. 1, pp. 23–48, February 1984.

[32] F. Rocca, C. Cafforio, and C. Prati, "Synthetic aperture radar: a new application for wave equation techniques," *Geophysical Prospecting*, vol. 39, pp. 809–830, 1989.

[33] C. Cafforio, C. Prati, and F. Rocca, "SAR data focusing using sysmic migration techniques," *IEEE Transactions on Aerospace and Electronic Systems*, vol. 27, no. 2, pp. 194–206, March 1991.

[34] M. Soumekh, "A system model an inversion for synthetic aperture radar imaging," *IEEE Transactions Image Processing*, vol. 1, no. 1, pp. 64–76, January 1992.